Glial metabolic states in human sporadic amyotrophic lateral sclerosis uncovered by spatial single-cell proteomics.

Momoka Hikosaka[1,9], Miyu Kinoshita[1,2,9], Kumiko Uemura[2,9], Md. Shamim Hossain[3,9], Masako Abe[4], Md Sorwer Alam Parvez[5], Siwakorn Punyawatthananukool[1,6], Mari Yoshida[7,*], Tatsuaki Tsuruyama[1,8,*], and Gen Ohtsuki[1,2,*]

[1] Department of Drug Discovery Medicine, Graduate School of Medicine, Kyoto University, Kyoto, Japan
[2] Department of Neuroscience, Graduate School of Medicine, Kyoto University, Kyoto, Japan
[3] Division of Lipid Cell Biology, Institute of Rheological Functions of Food, Fukuoka, Japan
[4] Division of Advanced Biomedicine, Medical Research Support Center, Graduate School of Medicine, Kyoto University, Kyoto, Japan
[5] Department of Psychiatry and Behavioral Neurobiology, Heersink School of Medicine, University of Alabama at Birmingham, Alabama, USA
[6] Department of Pharmacology, Faculty of Medicine Siriraj Hospital, Mahidol University, Bangkok, Thailand
[7] Department of Neuropathology, Institute for Medical Science of Aging, Aichi Medical University, Aichi, Japan
[8] Department of Clinical Laboratory, Kyoto Tachibana University, Kyoto, Japan
[9] These authors contributed equally.

*Correspondence: myoshida@aichi-med-u.ac.jp, tsuruyam@ddm.med.kyoto-u.ac.jp, and ohtsuki.gen.7w@kyoto-u.ac.jp

Supplementary Information

Supplementary Discussion

GFAP Expression and Astrocyte Heterogeneity in Sporadic ALS

Astrocytes express glial fibrillary acidic protein (GFAP), a type III intermediate filament protein, essential for astrocyte maturation and structural integrity. In central nervous system (CNS) inflammation, GFAP expression is markedly upregulated in reactive astrocytes, a characteristic feature of gliosis observed in multiple neurodegenerative diseases, including ALS, Alzheimer's disease (AD), and Parkinson's disease (PD)[61, 62]. The reactive astrocyte response typically arises from neuronal injury or degeneration. In ALS, GFAP-positive astrocytes are prominently found in the motor cortex and spinal cord, whereas in AD, GFAP expression is most evident in astrocytes surrounding amyloid plaques.

Under physiological conditions, GFAP is nearly undetectable in the blood. However, CNS injury may lead to astrocyte activation and/or disruption, permitting GFAP to leak into the extracellular space and enter systemic circulation. Furthermore, partial disruption of the blood-brain barrier (BBB), frequently reported in neurodegenerative conditions such as AD, PD, and multiple sclerosis, may further facilitate this peripheral increase in GFAP levels[63, 64]. Indeed, elevated serum GFAP has been proposed as a peripheral biomarker for CNS pathology. Verde et al. (2023)[64] demonstrated that serum GFAP concentrations in ALS patients were significantly higher (117.0 pg/mL) than in controls (92.1 pg/mL), highlighting its potential diagnostic value. However, despite this trend, GFAP levels do not uniformly reflect astrocyte reactivity or dysfunction. Certain astrocyte subtypes, including protoplasmic and interlaminar astrocytes, naturally express low or variable GFAP levels. Controversially, during early disease stages or within specific brain regions, GFAP expression may remain low even in the presence of pathological alterations.

Consistent with this heterogeneity, our study identified a GFAP-low astrocyte cluster in the early-stage ALS precentral gyrus (Fig. 2 and *inset* Figures 1A and B), aligning with previous transcriptomic findings reporting reduced *GFAP* gene expression in sporadic ALS (sALS) astrocytes (*inset* Figure 1C) (Pineda et al., 2024)[31] and AD astrocytes[65]. In particular, the disease-associated astrocyte subpopulation (Astro_1 in Fig. 2) belongs to this GFAP-low category. Importantly, GFAP downregulation occurred independently of pTDP-43, GLS, and IL6ST upregulation, indicating that GFAP-low expression does not exclude a degenerative or reactive astrocyte phenotype. Disrupted astrocytes may leak GFAP protein, leading to reduced expression in immunohistochemistry. Nevertheless, this study has several limitations, including the restricted number of proteins detectable by IMC and a limited sample size, which confines the generalization of our findings.

Taken together, these findings suggest that the relationship between GFAP expression, at RNA and protein levels, and gliosis in sALS is not linear and may vary depending on astrocyte subtype, disease stage, brain region, and molecular context. While GFAP remains a useful marker for certain aspects of astrocyte reactivity, its limitations must be considered in studies of neurodegeneration within parenchyma and in the interpretation of biomarker data from peripheral fluids.

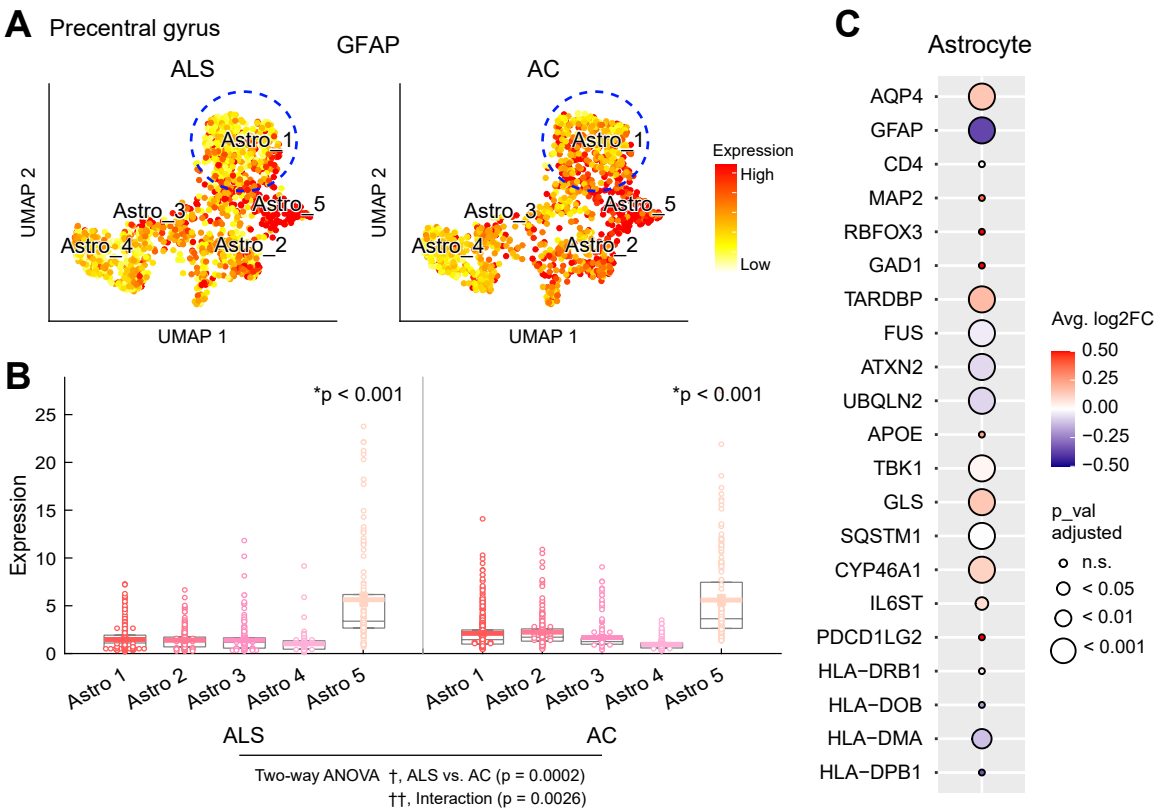

Inset Figure 1. Reduced GFAP levels in IMC ALS disease cluster and scRNA data.

(A, B) UMAP plots showing GFAP expression in astrocyte clusters from the precentral gyrus IMC (A), and GFAP expression levels across astrocyte subpopulations (B). GFAP protein expression is decreased in ALS astrocytes. ALS-associated subpopulations (Astro_1, Fig. 2c) exhibited low GFAP expression; however, GFAP levels did not consistently correlate with the expression of other ALS-associated proteins. A two-way ANOVA was conducted to assess differential expression across subclusters ($F(4, 2505) = 232.57$, $^{*}p < 0.0001$) and the AC-ALS factor ($F(1, 2505) = 13.79$, $^{\dagger}p = 0.0002$). The results suggest that GFAP expression is significantly reduced in ALS compared to that in AC. The interaction effect (subclusters × AC-ALS factor, $F(4, 2505) = 4.11$, $^{\dagger\dagger}p = 0.0026$) also indicated that the reduction in GFAP was overly expressed than expected from expression dynamics of other molecules, highlighting an ALS-specific regulatory mechanism influencing GFAP protein levels.

(C) Disease-induced changes in RNA expression in astrocytes. Using publicly available RNA-seq data (Supplementary Fig. 1) (Pineda et al., 2024)[31], we examined differential expression of the genes encoding the markers used for imaging mass cytometry (IMC). Cells with insufficient transcript expression levels were excluded from analysis. Note that *GFAP* expression was downregulated in ALS astrocytes, consistent with the reduced protein-level findings in ALS.

Mitochondrial Genes and TP53-Related Pathways in ALS

Our analysis of publicly available single-cell RNA sequencing data revealed a metabolic gene signature under the regulation of *TP53* (Supplementary Fig. 1c, d), consistent with prior studies implicating p53 activity in ALS pathology[58, 59, 66]. Within this signature, *MT-CO1* and *MT-CO3*, encoding cytochrome c oxidase subunits I and III, emerged as notable components. These subunits form part of Complex IV in the mitochondrial respiratory chain, which transfers electrons to molecular oxygen and plays a central role in oxidative phosphorylation.

The involvement of these mitochondrial genes is indispensable, given the widespread recognition of mitochondrial dysfunction in neurodegeneration. However, high mitochondrial transcript content is often used as a proxy for cellular stress or apoptosis in single-cell analyses, and cells exceeding a defined threshold are typically excluded. In our re-analysis, we followed a 10% threshold for mitochondrial gene expression in human samples, in line with current standards [67]. Even within these parameters, *MT-CO1* and *MT-CO3* were consistently upregulated in sporadic ALS samples compared to non-pathogenic age-matched controls (Supplementary Figs. 1d, 3a, and 3b). This suggests that mitochondrial metabolic alterations may intersect with *TP53* signaling pathways in ALS. One possible mechanism is via the release of mitochondrial DNA or other danger signals that activate the cGAS/STING pathway [68], or through disturbed communication between mitochondrial and lysosomal processes, linked to inflammatory signaling, reactive oxygen species production, calcium dysregulation, and eventual cell death [69–72].

Although these findings do not establish causality, they support the hypothesis that mitochondrial gene dysregulation may contribute to the cellular stress responses observed in ALS. These results also call for careful reconsideration of standard filtering practices in transcriptomic analyses, which may inadvertently exclude disease-relevant mitochondrial signals.

Supplementary Methods

Imaging mass cytometry

Tissue staining (Detailed version)

The staining procedure for tissue imaging for the Hyperion® imaging system (Standard BioTools) followed standard immunohistochemistry and immunofluorescence (IF) protocols for tissue collection, tissue processing, and staining. Imaging mass cytometry (IMC) was performed as described previously [46] with minor modifications for human brain and spinal cord tissues. Postmortem samples were obtained from patients with ALS and non-ALS control participants who, based on clinical data and treatment history, had no diagnosed motor or cognitive impairments in life. These samples were used for both IMC, hematoxylin and eosin (H&E) staining, and IF experiments. After perfusion and fixation with 10% formalin, brains were kept in formalin for two days at 4°C. Then, brain tissues were dehydrated, degreased, and embedded in paraffin. Paraffin-embedded tissue blocks were sectioned by 4-μm thickness, attached to a glass slide, and dried at 37°C for 24 hours. We took brain samples from the precentral gyrus, the anterior horn of lumbar spinal cord, and the cerebellar cortex of 12 participants (6 ALS patients and 6 aged non-ALS controls). After stretching paraffin with a slide-oven, sections were dewaxed in fresh xylene for 20 min (FUJIFILM Wako Pure Chemical Co., Osaka, Japan), and the slides were hydrated in descending grades of ethanol for deparaffinization. After incubation with antigen retrieval solution (Antigen Retrieval Reagent pH 9.0 (10x), S236784-2 Agilent® for precentral gyrus and cerebellum; Citrate Buffer, pH 6.0, 10x, Antigen Retriever, C9999 Sigma-Aldrich for spinal cord) and immersion with 3% BSA (Bovine Serum Albumin, A3059, Sigma-Aldrich) blocking solution, the slides were placed in a hydration chamber, and the antibody master mix was applied onto the section enclosed with a PAP pen. Instead of using sterile water, we used Maxpar Water and Maxpar PBS (Standard BioTools: 201069 and 201058, respectively) to prevent contamination of a very small amount of metal ingredients. Tissues on the slides were incubated overnight with the antibody cocktail at 4°C in a hydration chamber. Afterward, slides were washed in 0.2% Triton X-100 in Maxpar PBS and Maxpar PBS. Lastly, for nuclear staining, the tissues were stained with Intercalator-Ir (Cell-ID™ Intercalator-Ir, Standard BioTools: 201192A) in Maxpar PBS (80 μL/section of 1:400 diluted

solution) for 30 min at room temperature in a hydration chamber.

The antibody cocktail was custom-designed for this study's aim and composed of antibodies: Anti-Aquaporin 4 antibody [EPR24281-65] - BSA and Azide free (Rabbit monoclonal antibody, abcam: ab282586, RRID: AB_2923003), p62/SQSTM1 Antibody (2C11) (Mouse monoclonal antibody, NovusBio: H00008878-M01, RRID: AB_548364), Ubiquilin 2 Antibody (5F5) (Mouse monoclonal antibody, Novusbio: H00029978-M03, RRID: AB_828835), Anti-Glutaminase antibody [EP7212] - BSA and Azide free (Rabbit monoclonal antibody, abcam: ab214802, RRID: AB_3695649), Anti-NeuN antibody [EPR12763] - BSA and Azide free (Rabbit monoclonal antibody, abcam; ab209898, RRID: AB_3695640), Anti-MAP2 antibody - Neuronal Marker (Rabbit polyclonal antibody, abcam: ab32454, RRID: AB_776174), ATXN2 antibody [HL1902] (Rabbit monoclonal antibody, GeneTex: GTX637651, RRID: AB_3695642), Anti-LINE-1 ORF1p antibody [EPR22227-6] - BSA and Azide free (Rabbit monoclonal antibody, abcam: ab246317, RRID: AB_3695652), Anti TDP-43, phospho Ser409/410 (Mouse monoclonal antibody, Cosmo Bio: TIP-PTD-M01A, RRID: AB_3695645), Anti-CYP46A1 antibody [1A7] - BSA and Azide free (Mouse monoclonal antibody, abcam: ab255757, RRID: AB_3695655), GFAP Polyclonal Antibody (Rabbit polyclonal antibody, Invitrogen: PA1-9565, RRID: AB_2109797), Anti-gp130/IL6ST Antibody (Rabbit polyclonal antibody, Sino Biological: 101867-T10, RRID: AB_3094604), IBA1 Monoclonal Antibody (HL22-MS) (Mouse monoclonal antibody, Invitrogen: MA5-38265, RRID: AB_2898181), Anti-CX3CR1 antibody (Rabbit polyclonal antibody, abcam: ab8020, RRID: AB_306202), Phospho-TBK1/NAK (Ser172) (D52C2) XP® Rabbit mAb (BSA and Azide Free) (Rabbit monoclonal antibody, Cell Signaling: 54382, RRID: AB_3695654), TMEM119 (E3E4T) Mouse mAb (BSA and Azide Free) (Mouse monoclonal antibody, Cell Signaling Technology: 83308, RRID: AB_3695648), Anti-GAD67 antibody [GAD1/2563] - BSA and Azide free (Mouse monoclonal antibody, abcam: ab237842, RRID: AB_3695650), FUS Polyclonal Antibody (Rabbit polyclonal antibody, Invitrogen: PA5-23696, RRID: AB_2541196), Anti-Choline Acetyltransferase antibody [EPR13024(B)] - BSA and Azide free (Rabbit monoclonal antibody, abcam: ab224267, RRID: AB_3695651), Anti-Apolipoprotein E antibody [D6E10] - BSA and Azide free (Mouse monoclonal antibody, abcam: ab1906, RRID: AB_302668), TREM2 Antibody [clone TREM2/7210] (V9417) (Mouse monoclonal antibody, NSJ Bio: V9417SAF, RRID: AB_3094605), Anti-MHC Class II antibody [6C6] (Mouse monoclonal antibody, abcam: ab55152, RRID: AB_944199), Anti-TDP43 antibody [EPR18554] - BSA and Azide free (Rabbit monoclonal antibody, abcam: ab238443, RRID: AB_3695644), Monoclonal Mouse anti-Human NAK / TBK1 Antibody (Mouse monoclonal antibody, LifeSpan BioSciences: LS-C368304, RRID: AB_3695653). BSA-, glycerol-, and azide-free antibodies were selected as possible for higher imaging quality and sensitivity. We also used commercially available meta-conjugated antibodies: Anti - Human FoxP3 (PCH101) - 155Gd (Standard Biotools: 3155018D, RRID: AB_3106908), Anti - Human PD - 1 (EPR4877(2)) - 165Ho (Standard Biotools: 3165039D, RRID: AB_3106909), Anti - Human PD - L1 (E 1 L3N) - 150Nd (Standard Biotools: 3150031D, RRID: AB_3678081), Anti - Human PD - L2 (D7U8C) - 172Yb (Standard Biotools: 3172031D, RRID: AB_3678138), Anti - CD8a (C8 / 144B) - 167Er (Standard Biotools: 91H015167, RRID: AB_3678195), and Anti - CD4 (EPR6855) - 163Dy (Standard Biotools: 91H010163, RRID: AB_3678178).

We selected the antibodies listed above to visualize various cell types: neurons (NeuN, MAP2), inhibitory neurons (GAD67), cholinergic neurons (ChAT), astrocytes and the blood-brain barrier (GFAP, AQP4), microglia (IBA1, CX3CR1, TMEM119), antigen-presenting cells (MHC class II), helper T cells (CD4), cytotoxic T cells (CD8), and regulatory T cells (FoxP3). To assess

cellular function, we used TREM2 as a marker for disease-associated cells. For ALS-specific markers, we used pTDP-43, FUS, ATXN2, and UBQLN2. TDP-43, an RNA-binding protein, serves as the non-phosphorylated counterpart of pTDP-43. APOE was used to examine lipid metabolism; p62/SQSTM1, a ubiquitin-binding protein, served as a marker for autophagosome cargo; and glutaminase (GLS) was used as a marker for glutamine metabolism. We also assessed ORF1 (LINE-1), a retrotransposable element; CH24H (CYP46A1), involved in cholesterol metabolism; and IL6ST (gp130, CD130), an inflammatory cytokine signal transducer. Phosphorylated TBK1 (Ser172) is involved in IκB kinase (IKK) and NF-κB signaling, while TBK1 more broadly is associated with cell proliferation, apoptosis, autophagy, autoimmunity, and anti-tumor immunity. Finally, PD-1, PD-L1, and PD-L2 were included to investigate immune checkpoint pathways. We conducted pilot staining using one aged control (N = 1) and one ALS case (N = 1) to determine the optimal concentrations of metal-conjugated antibodies for IMC. For each brain region, we tested three different antibody concentrations and two antigen retrieval conditions. Note that the antibody concentrations recommended by manufacturers for immunohistochemistry may not be directly applicable to IMC, making rigorous quality control essential.

We manually conjugated each antibody to lanthanide (Ln) metals using Maxpar® X8 Antibody Labeling Kit (Standard BioTools), following the Maxpar Antibody Labeling User Guide (PRD002 Rev 17, Chapter 3: Maxpar X8 Antibody Labeling Kits). Briefly, the Ln metal solution was loaded onto Maxpar X8 polymer, and the antibodies were partially reduced with TCEP [Tris (2-carboxyethyl)phosphine hydrochloride (TCEP) solution, pH 7.0, 646547, Sigma-Aldrich]. Both the Ln-loaded polymer and the reduced antibody were conjugated. Ln metal solutions used in our study are as follows: Maxpar® X8 Antibody Labeling Kit 141Pr for AQP4, 201141A; 143Nd for p62/SQSTM1, 201143A; 145Nd for UBQLN2, 201145A; 147Sm for Glutaminase, 201147A; 149Sm for NeuN, 201149A; 150Nd for PD-L1, 201150A; 151Eu for MAP2, 201151A; 152Sm for ATXN2, 201152A; 153Eu for ORF1 (LINE-1), 201153A; 154Sm for pTDP-43, 201154A; 155Gd for FoxP3, 201155A; 156Gd for CH24H, 201156A; 158Gd for GFAP, 201158A; 159Tb for IL6ST, 201159A; 160Gd for IBA1, 201160A; 161Dy for CX3CR1, 201161A; 162Dy for pTBK1 (Ser172), 201162A; 163Dy for CD4, 201163A; 164Dy for TMEM119, 201164A; 165Ho for PD-1, 201165A; 166Er for GAD67, 201166A; 167Er for CD8, 201167A; 168Er for FUS, 201168A; 169Tm for ChAT, 201169A; 170Er for APOE, 201170A; 171Yb for TREM2, 201171A; 172Yb for PD-L2, 201172A; 174Yb for MHC class II, 201174A; 175Lu for TDP-43, 201175A; 176Yb for TBK1, 201176A. The final concentration of metal-conjugated antibodies are 141Pr-AQP4, 10 μg/ml; 143Nd-p62/SQSTM1, 15 μg/ml; 145Nd-UBQLN2, 20 μg/ml; 147Sm-Glutaminase, 15 μg/ml; 149Sm-NeuN, 25 μg/ml; 150Nd-PD-L1, 6 μg/ml; 151Eu-MAP2, 24 μg/ml; 152Sm-ATXN2, 15 μg/ml; 153Eu-ORF1 (LINE-1), 20 μg/ml; 154Sm-pTDP-43, 25 μg/ml; 155Gd-FoxP3, 6 μg/ml; 156Gd-CH24H, 17.5 μg/ml; 158Gd-GFAP, 30 μg/ml; 159Tb-IL-6ST, 15 μg/ml; 160Gd-IBA1, 20 μg/ml; 161Dy-CX3CR1, 6.9 μg/ml; 162Dy-pTBK1 (Ser172), 17.72 μg/ml; 163Dy-CD4, 3.5 μg/ml; 164Dy-TMEM119, 20 μg/ml; 165Ho-PD-1, 5 μg/ml; 166Er-GAD67, 20 μg/ml; 167Er-CD8, 3.5 μg/ml; 168Er-FUS, 10 μg/ml; 169Tm-ChAT, 25 μg/ml; 170Er-APOE, 10 μg/ml; 171Yb-TREM2, 20 μg/ml; 172Yb-PD-L2, 6 μg/ml; 174Yb-MHC class II, 10 μg/ml; 175Lu-TDP-43, 20 μg/ml; 176Yb-TBK1, 15 μg/ml. We determined the final concentration of metal-conjugated antibodies from the IMC image of one experiment across the brain (precentral gyrus, spinal cord, and cerebellum) by conducting the IMC imaging with three different concentrations of metal-conjugated antibodies and different retrieval conditions (pH 9.0 or 6.0), as mentioned above.

Cell segmentation and clustering (additional information)

For cell segmentation, we used Cell Profiler v4.2.1 [73]. The histoCAT-analysis provides clustering at the single-cell level [74] and normalized expression. Downstream analyses were performed primarily using the Seurat package [75] in R. We identified 12,181, 7,956, 16,343, and 38,852 cells from precentral gyrus gray matter, white matter, spinal cord, and cerebellum, respectively. Prior to clustering, batch-effect correction was applied using Harmony [76] within the brain region. To improve the refinement of single-cell detection, we developed a custom MATLAB-code and corrected erroneous identification, semi-manually (*inset* Figure 2).

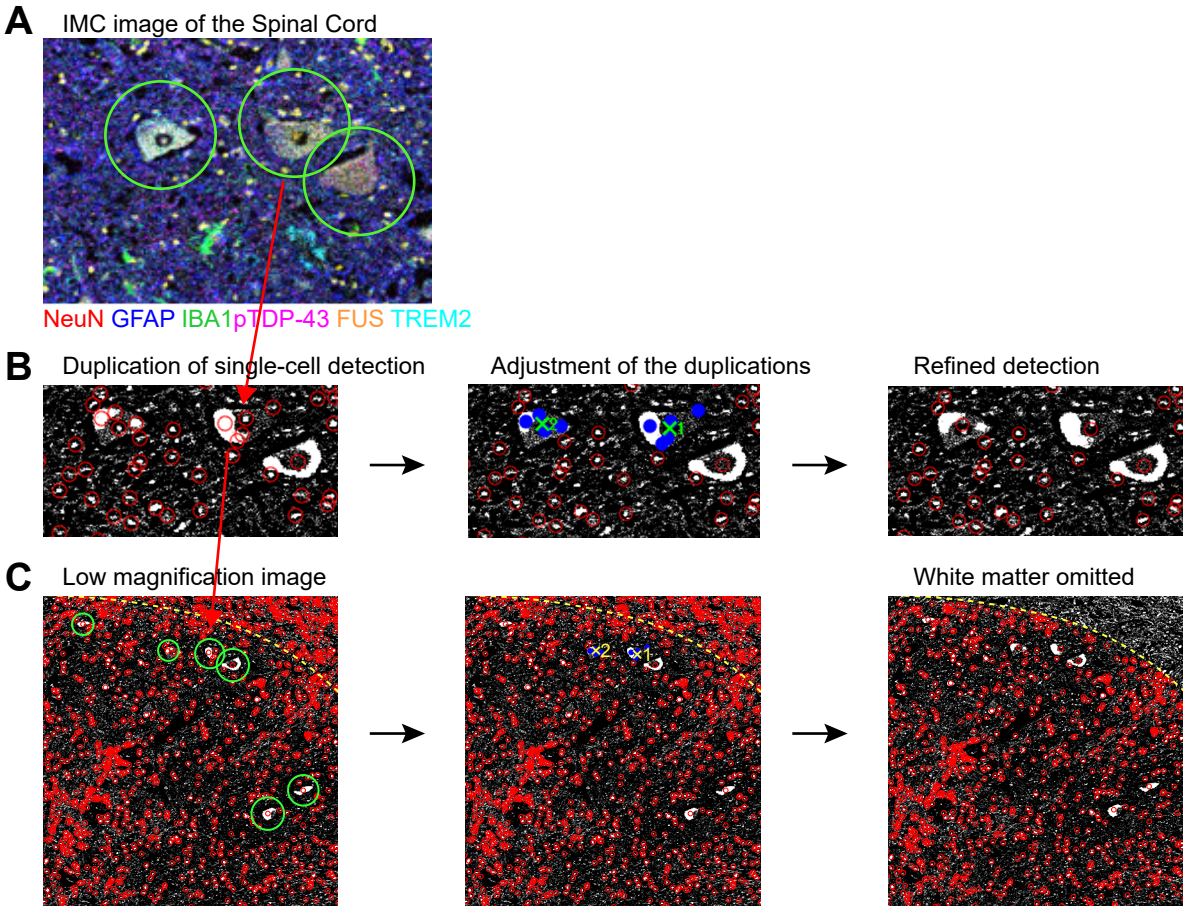

***Inset* Figure 2. Programming-assisted correction of cell identification**

***Inset* Figure 2 legend:**

For refinement of single-cell identification with Cell Profiler v4.2.1 and histoCAT, we adopted the analysis pipeline to maximize cell-identification accuracy. In human samples, Cell-ID™ Intercalator-Ir signals did not always reliably mark nuclear positions, particularly in large cells in which DNA had leaked from the nuclear membrane into the cytosol, likely due to fixation conditions or specimen preservation. We therefore re-evaluated our initial cell-identification results and confirmed the presence of such cases.

For example, in spinal cord samples, large neurons (green circles in panel A) showed diffuse Intercalator-Ir signals distributed throughout the cytoplasm (white signal in panel B), rather than being confined to the nucleus. This led to multiple detections within a single cell, requiring post hoc correction. To address this issue, we developed a custom MATLAB-based computational

algorithm to identify multiple detections originating from the same cell (green circles in panel C) and recalculated a single centroid from the aggregated detection coordinates. The images on the right show corrected single-cell identification. Yellow dashed lines indicate the boundary between gray and white matter; cells within this region were excluded from the analysis. All the IMC data was corrected semi-manually in both the precentral gyrus (Fig. 2) and spinal cord (Fig. 3).

For trajectory reconstruction (Fig. 2d), we used Monocle 3 package (v1.3.7)[77]. The orientation of the start and end points was determined based on marker expression patterns. For enrichment analysis, we adopted Enrichr[78] and applied top 40 upregulated genes using Reactome Pathways 2024 (Supplementary Fig. 1c and 1d). For an alternative analysis of gene enrichment, we performed gene set enrichment analysis (GSEA)[79] in Supplementary Fig. 3.

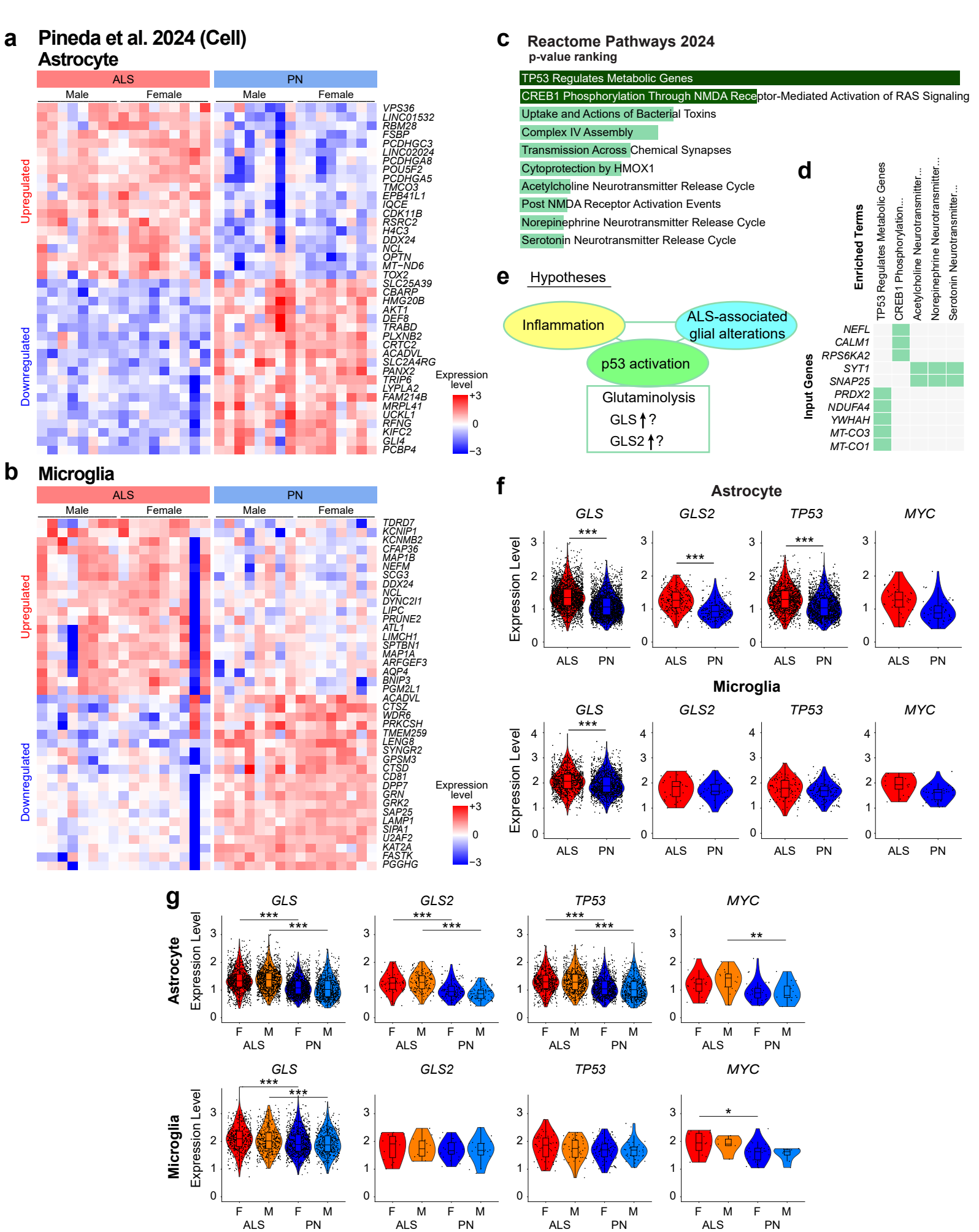
a
Pineda et al. 2024 (Cell)
Astrocyte
ALS
PN
Male
Female
Upregulated
Downregulated
VPS36
LINC01532
RBM28
FSBP
PCDHGC3
LINC02024
PCDHGA8
POU5F2
PCDHGA5
TMCO3
EPB41L1
IQCE
CDK11B
RSRC2
H4C3
DDX24
NCL
OPTN
MT-ND6
TOX2
SLC25A39
CBARP
HMG20B
AKT1
DEF8
TRABD
PLXNB2
CRTC2
ACADVL
SLC2A4RG
PANX2
TRIP6
LYPLA2
FAM214B
MRPL41
UCKL1
RFNG
KIFC2
GLI4
PCBP4
Expression level
+3
0
−3
b
Microglia
TDRD7
KCNIP1
KCNMB2
CFAP36
MAP1B
NEFM
SCG3
DDX24
NCL
DYNC2I1
LIPC
PRUNE2
ATL1
LIMCH1
SPTBN1
MAP1A
ARFGEF3
AQP4
BNIP3
PGM2L1
ACADVL
CTSZ
WDR6
PRKCSH
TMEM259
LENG8
SYNGR2
GPSM3
CTSD
CD81
DPP7
GRN
GRK2
SAP25
LAMP1
SIPA1
U2AF2
KAT2A
FASTK
PGGHG
c
Reactome Pathways 2024
p-value ranking
TP53 Regulates Metabolic Genes
CREB1 Phosphorylation Through NMDA Receptor-Mediated Activation of RAS Signaling
Uptake and Actions of Bacterial Toxins
Complex IV Assembly
Transmission Across Chemical Synapses
Cytoprotection by HMOX1
Acetylcholine Neurotransmitter Release Cycle
Post NMDA Receptor Activation Events
Norepinephrine Neurotransmitter Release Cycle
Serotonin Neurotransmitter Release Cycle
d
Enriched Terms
TP53 Regulates Metabolic Genes
CREB1 Phosphorylation...
Acetylcholine Neurotransmitter...
Norepinephrine Neurotransmitter...
Serotonin Neurotransmitter...
Input Genes
NEFL
CALM1
RPS6KA2
SYT1
SNAP25
PRDX2
NDUFA4
YWHAH
MT-CO3
MT-CO1
e
Hypotheses
Inflammation
ALS-associated glial alterations
p53 activation
Glutaminolysis
GLS ↑?
GLS2 ↑?
f
Astrocyte
GLS
GLS2
TP53
MYC
Expression Level
***
ALS
PN
Microglia
GLS
GLS2
TP53
MYC
Expression Level
***
ALS
PN
g
Astrocyte
GLS
GLS2
TP53
MYC
Expression Level
***
**
F
M
ALS
PN
Microglia
GLS
GLS2
TP53
MYC
Expression Level
***
*
F
M
ALS
PN

Supplementary Fig. 1 | Glial upregulation of the glutaminase gene and involvement of TP53 in regulating different cell types.

a,**b**, Expression levels in ALS and pathologically normal (PN) brain single-cell transcriptome data (from 17 ALS and 16 PN individuals, 117,781 cells from Pineda et al. (2024)[31]). Upregulated and downregulated genes in astrocytes (**a**) and microglia (**b**) are shown in heatmaps.

c, Association of *TP53*-regulation with ALS-upregulated genes by Enrichr, Reactome pathways 2024.

d, A diagram illustrating specific genes and enrichment terms.

e, Hypotheses for ALS pathology, proposing the involvement of p53, the protein encoded by the *TP53* gene, in glutaminolysis, disease-associated glia, and inflammation.

f, Increases in *GLS* and *TP53* RNA expression in ALS cortical astrocytes and microglia. Statistical significance was determined using the Wilcoxon rank-sum test with false discovery rate (FDR) correction (***$p < 0.0001$).

g, Comparative expression of *GLS*, *GLS2*, *TP53*, and *MYC* between females and males. Statistical significance was determined using one-way ANOVA followed by Tukey-Kramer test. Asterisks indicate significant differences between groups (*$p < 0.05$; **$p < 0.01$; ***$p < 0.001$).

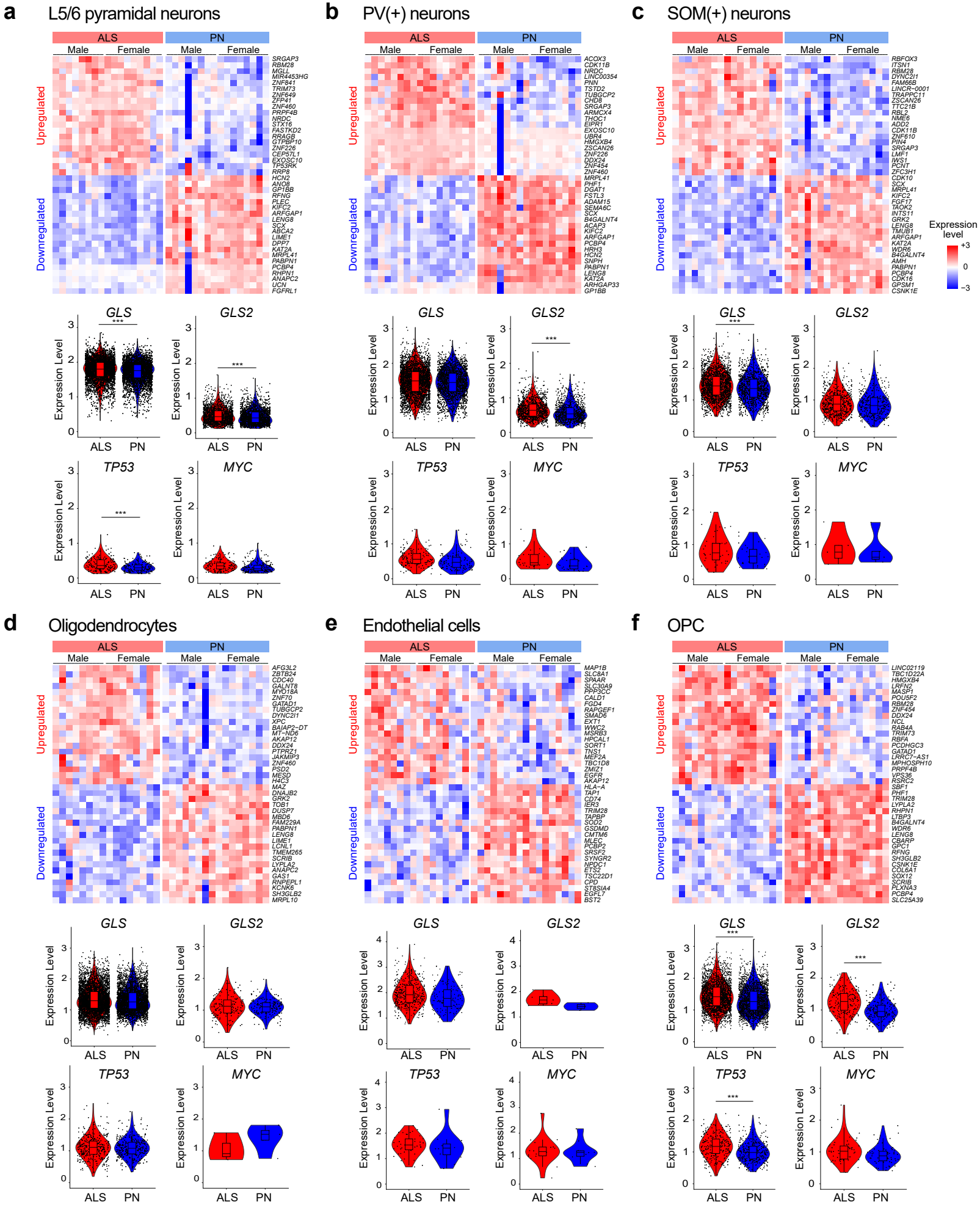
a
L5/6 pyramidal neurons
b
PV(+) neurons
c
SOM(+) neurons
d
Oligodendrocytes
e
Endothelial cells
f
OPC
ALS
PN
Male
Female
Upregulated
Downregulated
Expression level
+3
0
−3
GLS
GLS2
TP53
MYC
Expression Level
***

Supplementary Fig. 2 | Gene expression patterns across cell types from Pineda et al. (2024) [31].

a–f, Expression levels from publicly available single-cell transcriptomic data of sporadic ALS and pathologically normal (PN) brains are presented. Heatmaps display upregulated and downregulated genes in L5/6 pyramidal neurons (**a**), PV(+) interneurons (**b**), SOM(+) interneurons (**c**), oligodendrocytes (**d**), endothelial cells (**e**), and oligodendrocyte progenitor cells (OPCs) (**f**). RNA expression levels of *GLS*, *GLS2*, *TP53*, and *MYC* in ALS and PN cortical samples are shown below each plot. Asterisks denote significant differences as determined by the Wilcoxon rank-sum test with false discovery rate (FDR) correction (***$p < 0.0001$).

.

a

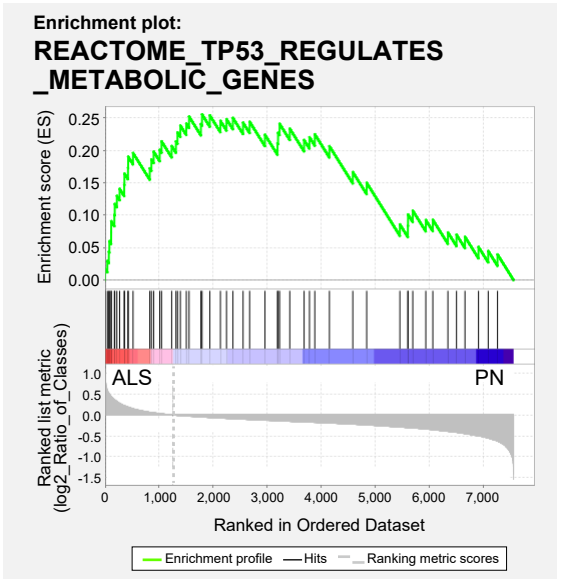

b

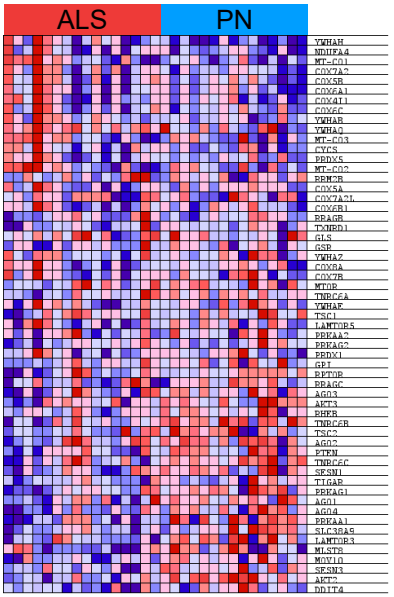

Core Enrichment Genes

YWHAH NDUFA4 MT-CO1 COX7A2 COX5B COX6A1 COX4I1 COX6C YWHAB YWHAQ MT-CO3 CYCS PRDX5 MT-CO2 RRM2B COX5A COX7A2L COX6B1 RRAGB TXNRD1 GLS GSR YWHAZ COX8A COX7B MTOR TNRC6A YWHAE

c

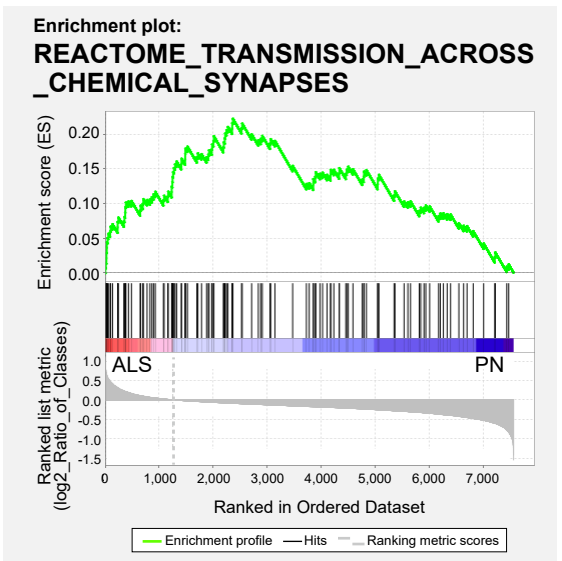

d

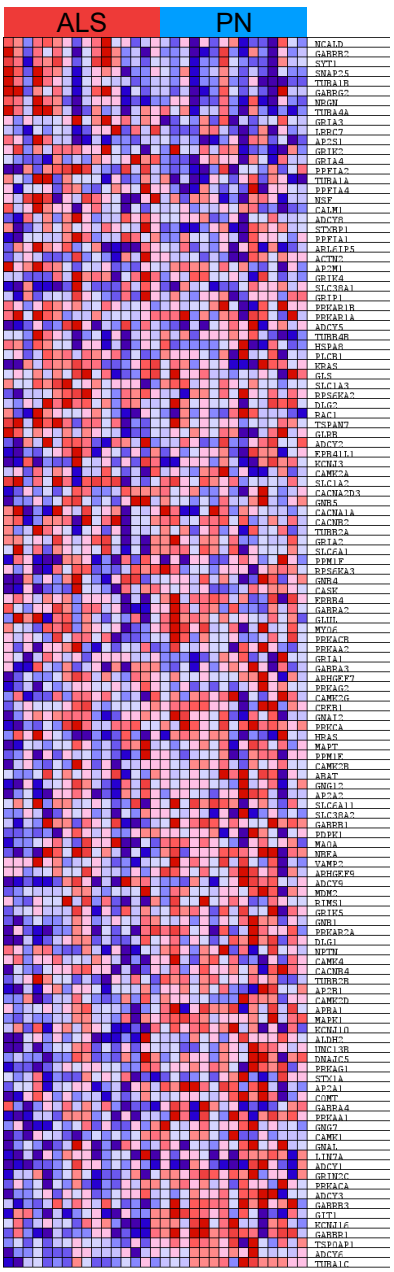

Core Enrichment Genes

NCALD GABRB2 SYT1 SNAP25 TUBA1B GABRG2 NRGN TUBA4A GRIA3 LRRC7 AP2S1 GRIK2 GRIA4 PPFIA2 TUBA1A PPFIA4 NSF CALM1 ADCY8 STXBP1 PPFIA1 ARL6IP5 ACTN2 AP2M1 GRIK4 SLC38A1 GRIP1 PRKAR1B PRKAR1A ADCY5 TUBB4B HSPA8 PLCB1 KRAS GLS SLC1A3 RPS6KA2 DLG2 RAC1 TSPAN7 GLRB ADCY2 EPB41L1 KCNJ3 CAMK2A SLC1A2 CACNA2D3 GNB5 CACNA1A CACNB2 TUBB2A GRIA2 SLC6A1 PPM1F RPS6KA3 GNB4 CASK ERBB4 GABRA2 GLUL MYO6 PRKACB PRKAA2 GRIA1 GABRA3 ARHGEF7 PRKAG2

Supplementary Fig. 3 | Gene set enrichment analysis (GSEA) of astrocyte single-cell RNA-seq data.
a, Enrichment plot of astrocyte genes from Pineda et al. (2024)[31] for the REACTOME_TP53_REGULATES_METABOLIC_GENES pathway. Core enrichment genes are shown below with *GLS* marked in red. For an analysis of gene enrichment, we performed gene set enrichment analysis (GSEA)[79].
b, Blue-pink o' gram comparing ALS and PN samples in the gene set space of REACTOME_TP53_REGULATES_METABOLIC_GENES.
c, Enrichment plot of astrocyte genes for the REACTOME_TRANSMISSION_ACROSS_CHEMICAL_SYNAPSES pathway. Core enrichment genes are shown below.
d, Blue-pink o' gram in the REACTOME_TRANSMISSION_ACROSS_CHEMICAL_SYNAPSES.
Sporadic ALS (n = 16) and pathologically normal (PN) controls (n = 15) were compared.

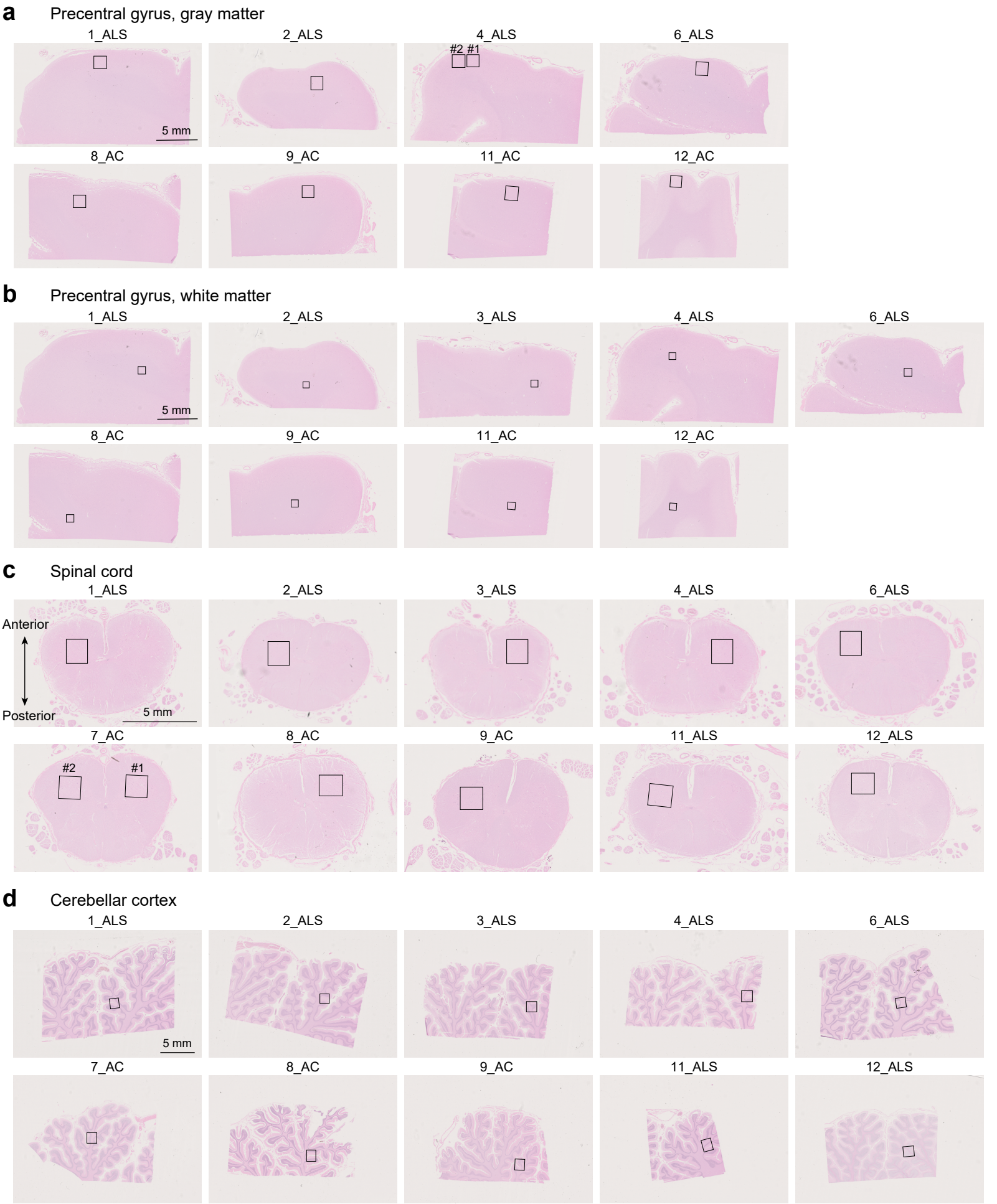
a
Precentral gyrus, gray matter
1_ALS
2_ALS
4_ALS
#2 #1
6_ALS
5 mm
8_AC
9_AC
11_AC
12_AC
b
Precentral gyrus, white matter
1_ALS
2_ALS
3_ALS
4_ALS
6_ALS
5 mm
8_AC
9_AC
11_AC
12_AC
c
Spinal cord
1_ALS
2_ALS
3_ALS
4_ALS
6_ALS
Anterior
Posterior
5 mm
7_AC
#2
#1
8_AC
9_AC
11_ALS
12_ALS
d
Cerebellar cortex
1_ALS
2_ALS
3_ALS
4_ALS
6_ALS
5 mm
7_AC
8_AC
9_AC
11_ALS
12_ALS

Supplementary Fig. 4 | Whole H&E-stained images of consecutive FFPE tissue sections used for IMC analysis in the precentral gyrus, anterior spinal cord and cerebellar cortex.

a, Whole H&E-stained images of gray matter in the precentral gyrus from individuals with ALS and non-ALS controls. Black squares indicate regions of interest (ROIs) selected for imaging mass cytometry (IMC).

b, Whole H&E-stained images of white matter in the precentral gyrus.

c, Whole H&E-stained images of the anterior spinal cord.

d, Whole H&E-stained images of the cerebellar cortex.

a

Antibody	Function / Marker
NeuN	Neuron
MAP2	Neuron
GAD67	Inhibitory neuron
ChAT	Cholinergic neuron
GFAP	Astrocyte
AQP4	Astrocyte, BBB
IBA1	Microglia
CX3CR1	Microglia
TMEM119	Microglia
TREM2	Microglia, disease-associated
MHC class II	Antigen presenting cell
CD4	Helper T cell
CD8	Killer T cell
FOXP3	Regulatory T cell

Antibody	Function / Marker
pTDP-43	ALS marker
TDP-43	RNA-binding protein
FUS	ALS marker
APOE	Lipid metabolism
ATXN2	ALS marker
UBQLN2	ALS marker
p62/SQSTM1	Ubiquitin-binding protein, autophagosome cargo
GLS	Glutamine aminohydrolase enzyme
ORF-1 (LINE-1)	Retrotransposable element
CH24H (CYP46A1)	Cholesterol metabolism
IL6ST (gp130, CD130)	Inflammatory cytokine signal transducer
pTBK1 (Ser172)	IκB kinase (IKK) & NF-κB-activating kinase
TBK1	Cell proliferation, apoptosis, autophagy, autoimmune, and anti-tumor immunity
PD-1	Immune checkpoint
PD-L1	Immune checkpoint
PD-L2	Immune checkpoint

b

	#1 ALS	#2 ALS	#4 ALS	#6 ALS	#8 AC	#9 AC	#11 AC	#12 AC
Male / Female	Female	Female	Male	Male	Female	Female	Male	Male
ALS duration	10M	12M	20M	24M				
MCI		+						
Age	69	71	73	75	61	53	71	60

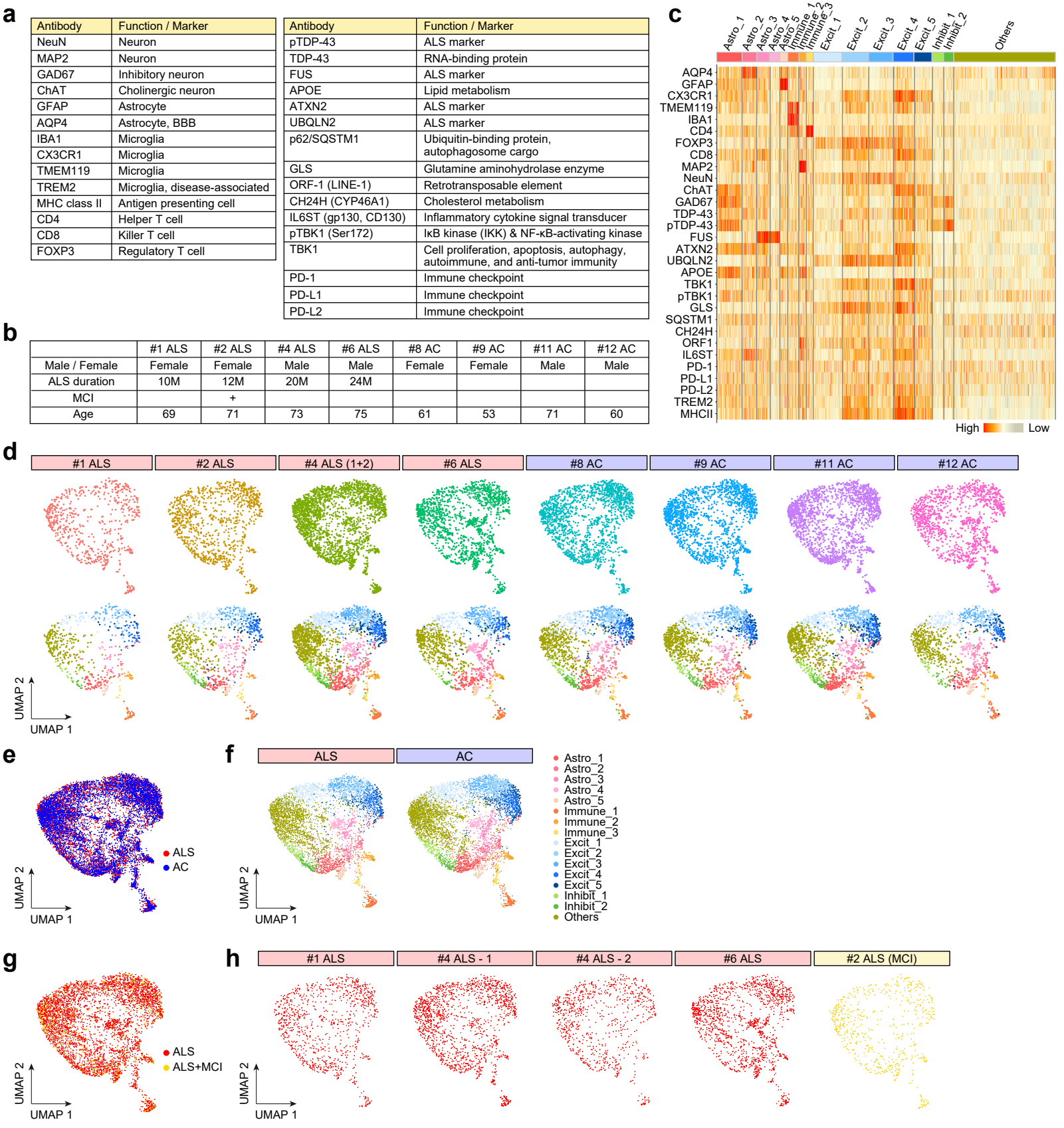

Supplementary Fig. 5 | General information on IMC markers, human samples, and cell features in the precentral gyrus.

a, List of antibodies used for imaging mass cytometry (IMC).

b, Basic and clinical information about individual participants who provided brain samples, including sex, ALS duration, mild cognitive impairment (MCI) status, and age at death. We followed rigorous neuropathological criteria when diagnosing and confirming each case of ALS/FTLD-TDP and age-related pathology [80, 81].

c, Normalized expression of markers across cells in the precentral gyrus. For Cell segmentation, we used Cell Profiler v4.2.1 [73]. The histoCAT-analysis provides clustering at the single-cell level [74] and normalized expression. Downstream analyses were performed primarily using the Seurat package [75] in R. We identified 12,181 cells from precentral gyrus gray matter. Prior to clustering, batch-effect correction was applied using Harmony [76] within the brain region (9 datasets for precentral gyrus gray matter).

d, UMAPs of individual single-cell data from the precentral gyrus (sporadic ALS vs. aged control (AC)) (*top*). UMAPs of reclustered cells for each individual brain are shown below.

e,**f**, Comparisons between ALS and AC.

g,**h**, Comparisons between ALS and MCI. Three ALS (red) and one ALS+MCI (yellow) are presented, with no distinct separation.

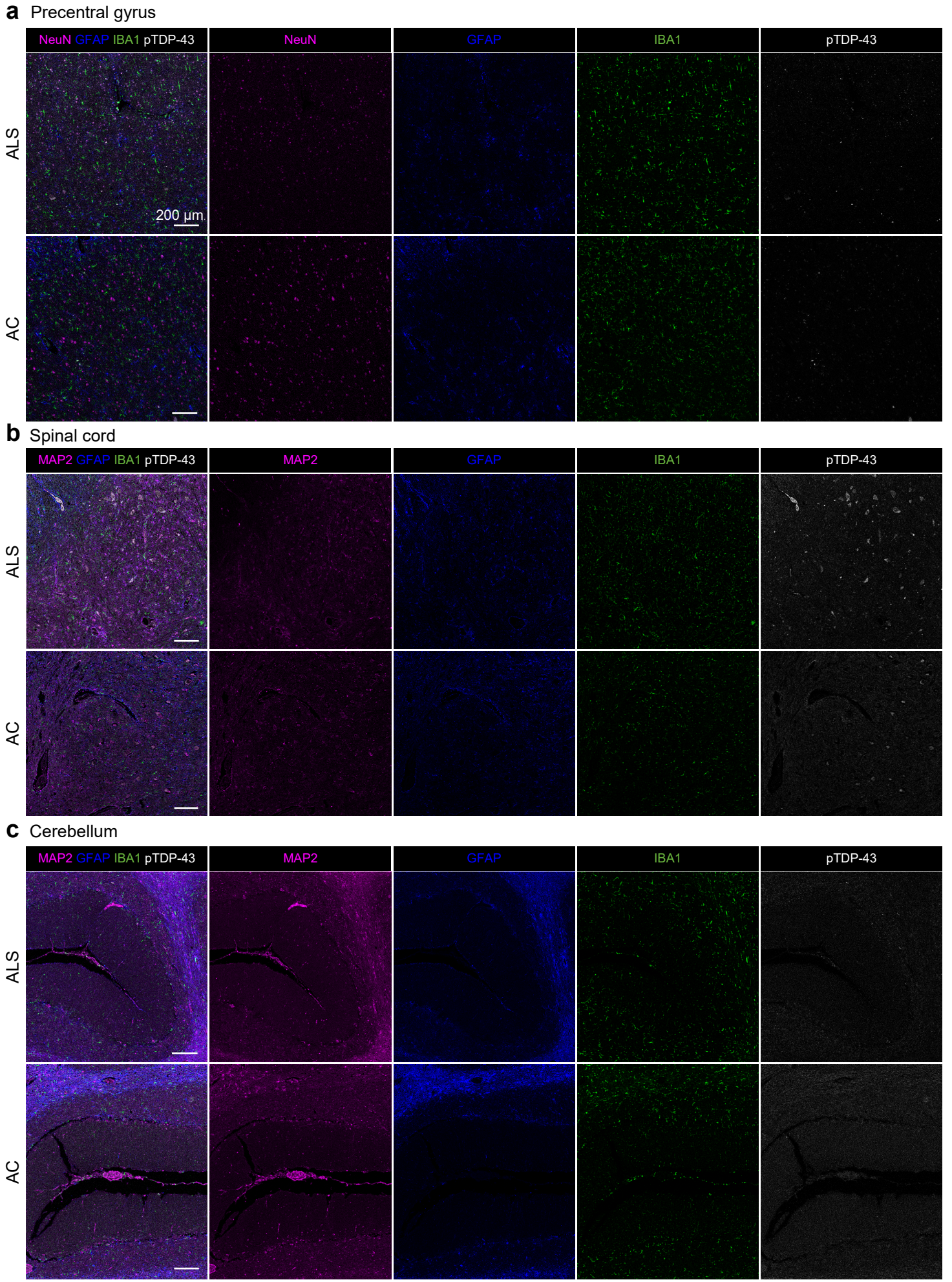
a Precentral gyrus
NeuN GFAP IBA1 pTDP-43
NeuN
GFAP
IBA1
pTDP-43
ALS
AC
200 μm
b Spinal cord
MAP2 GFAP IBA1 pTDP-43
MAP2
GFAP
IBA1
pTDP-43
ALS
AC
c Cerebellum
MAP2 GFAP IBA1 pTDP-43
MAP2
GFAP
IBA1
pTDP-43
ALS
AC

Supplementary Fig. 6 | Channel separation and magnified views of imaging mass cytometry.

a–c, Representative imaging mass cytometry images showing individual marker channels in the precentral gyrus (**a**), spinal cord (**b**), and cerebellum (**c**) (as in Fig. 1b). Markers include NeuN or MAP2, GFAP, IBA1, FUS, and pTDP-43 in ALS and AC samples.

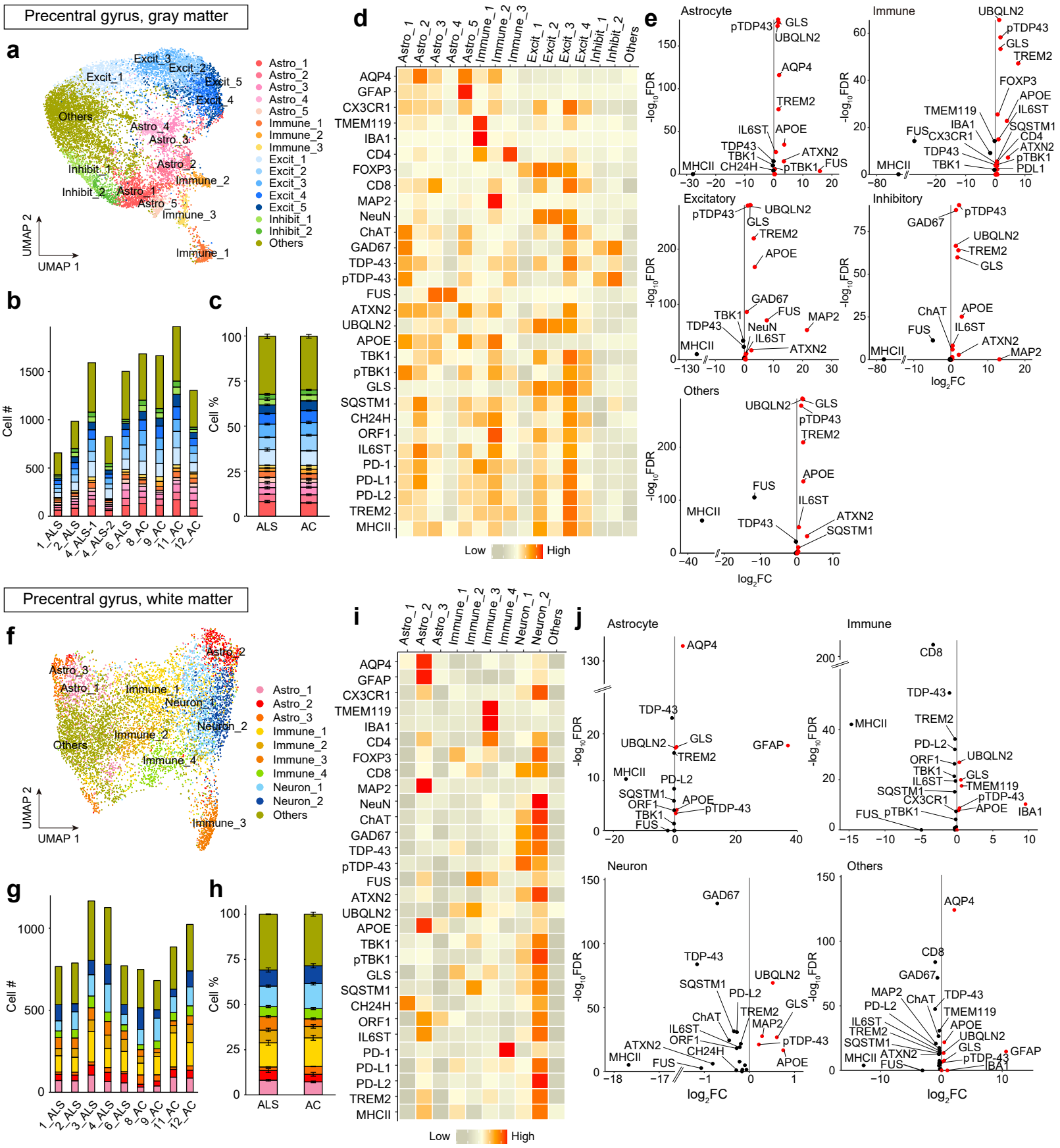

Supplementary Fig. 7 | Single-cell IMC subclassification of cortical gray and white matters.

a, UMAP of imaging mass cytometry (IMC) subclassification in the precentral gyrus gray matter.

b–d, Cell counts of annotated cell subtypes (**b**), cell proportions (mean ± SEM) (**c**), and marker expression heatmap in which values were Z-score-scaled per marker (**d**) in gray matter.

e, Volcano plots of marker protein intensity in astrocytes, immune cells, excitatory neurons, inhibitory neurons, and other populations.

f, UMAP of IMC subclassification in the precentral gyrus white matter.

g–i, Cell counts of annotated cell subtypes (**g**), cell proportions (mean ± SEM) (**h**), and marker expression heatmap, Z-score-scaled per marker (**i**) in white matter.

j, Volcano plots of marker protein intensity in astrocytes, immune cells, neurons, and other populations. Red dots indicate upregulated proteins, and black dots represent downregulated proteins (**e**, **j**).

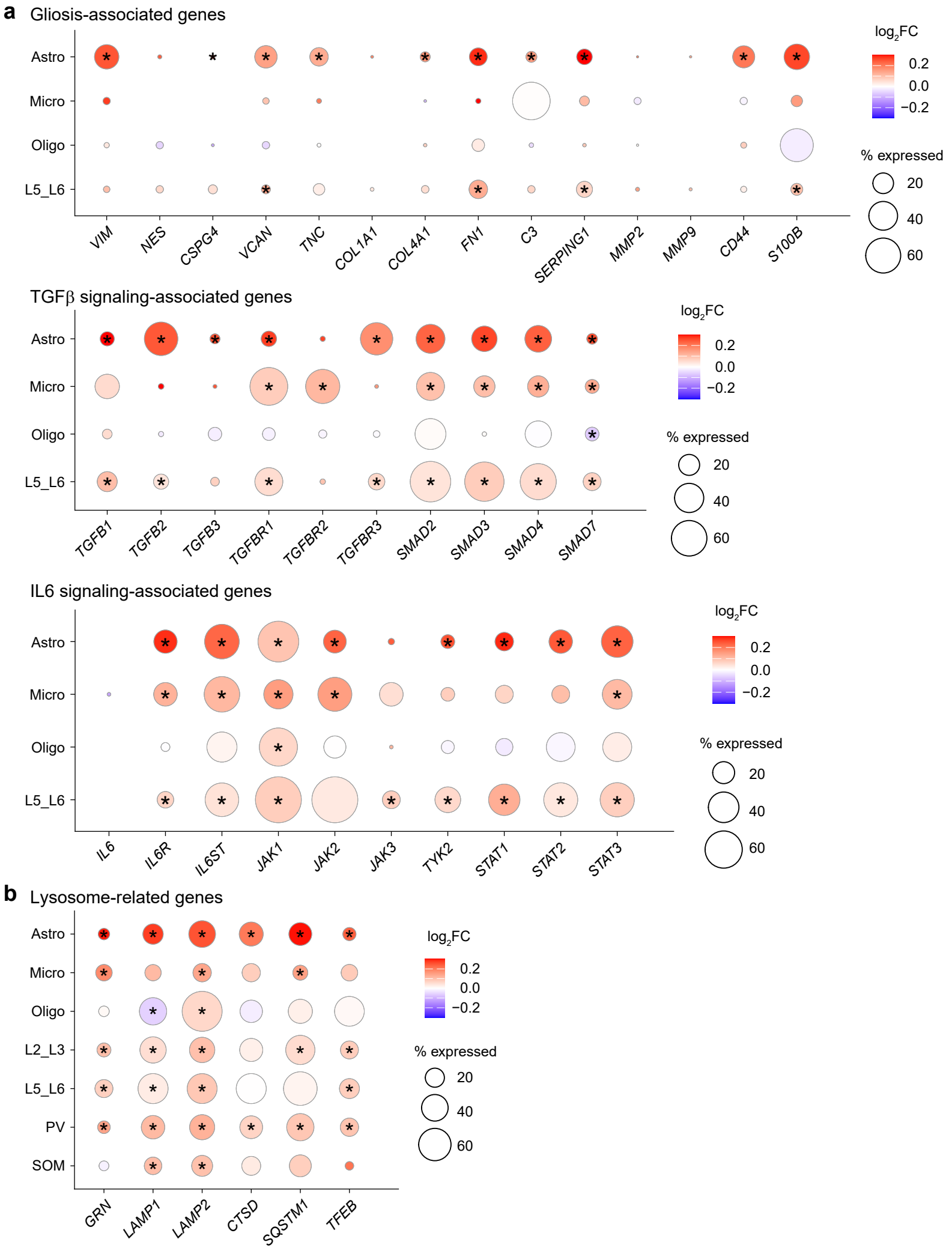
a
Gliosis-associated genes
Astro
Micro
Oligo
L5_L6
VIM
NES
CSPG4
VCAN
TNC
COL1A1
COL4A1
FN1
C3
SERPING1
MMP2
MMP9
CD44
S100B
log2FC
0.2
0.0
−0.2
% expressed
20
40
60
TGFβ signaling-associated genes
TGFB1
TGFB2
TGFB3
TGFBR1
TGFBR2
TGFBR3
SMAD2
SMAD3
SMAD4
SMAD7
IL6 signaling-associated genes
IL6
IL6R
IL6ST
JAK1
JAK2
JAK3
TYK2
STAT1
STAT2
STAT3
b
Lysosome-related genes
L2_L3
PV
SOM
GRN
LAMP1
LAMP2
CTSD
SQSTM1
TFEB

Supplementary Fig. 8 | Gliosis- and lysosome-related gene expression in the sALS motor cortex.

a, Dot plots of gliosis-, TGF-β signalling-, and IL6 signalling-related genes from Pineda et al. (2024)[31]. Expression patterns compared to pathologically-negative data are shown. Statistical significance was determined using the Wilcoxon ranksum test (*$p < 0.0001$).

b, Dot plots of lysosome-related genes from Pineda et al. (2024)[31]. Expression patterns compared to pathologically-negative data are shown. Statistical significance was determined using the Wilcoxon ranksum test (*$p < 0.0001$).

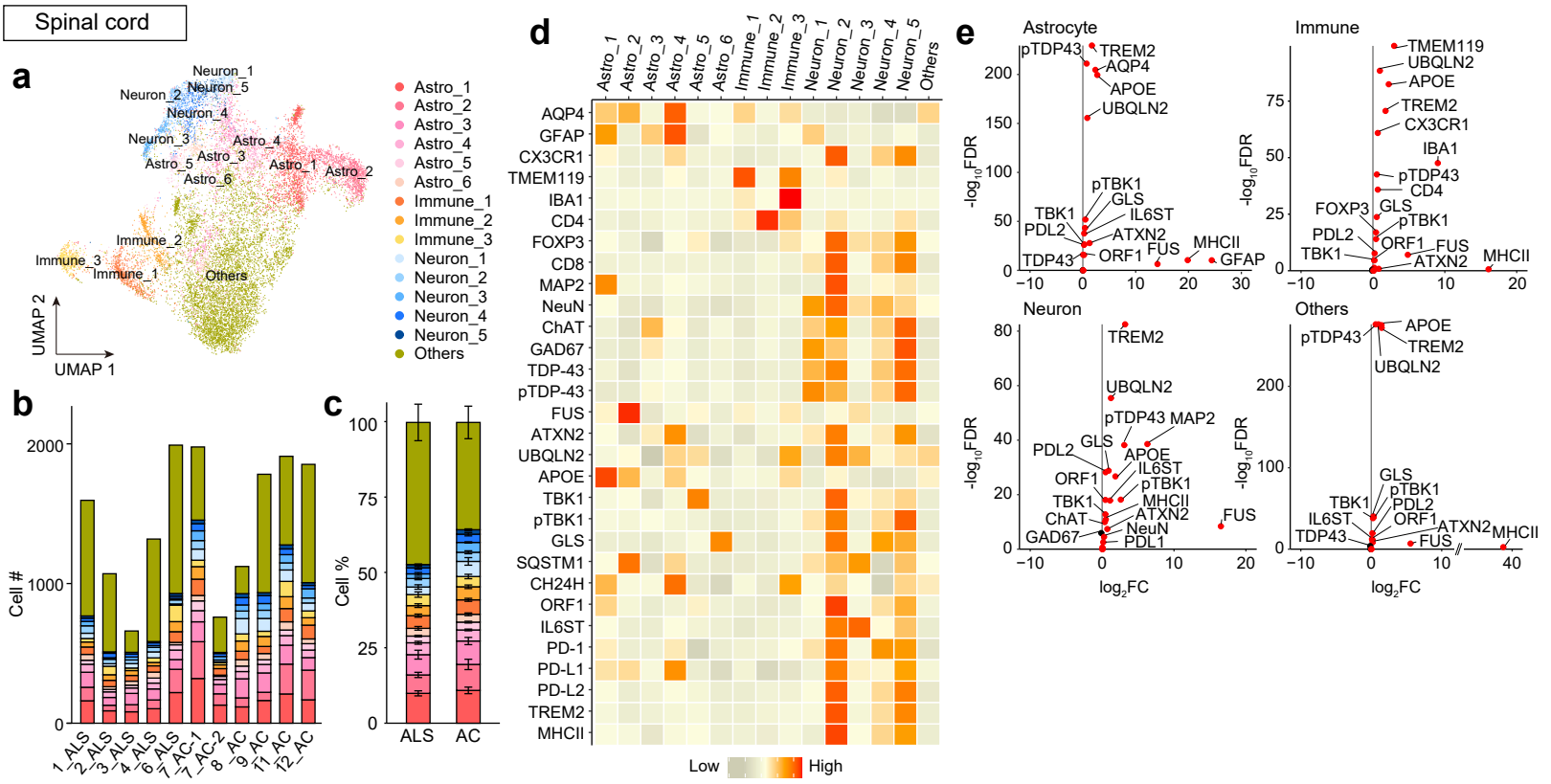

Supplementary Fig. 9 | Single-cell IMC subclassification of the spinal cord.

a, UMAP of IMC-based subclassification in the spinal cord.

b–d, Cell counts of annotated subtypes (**b**), cell proportions (mean ± SEM) (**c**), and marker expression heatmap in which values were Z-score-scaled per marker (**d**) in the spinal cord.

e, Volcano plots of marker protein intensity in astrocytes, immune cells, neurons, and other populations. Red dots indicate upregulated proteins; black dots represent downregulated proteins.

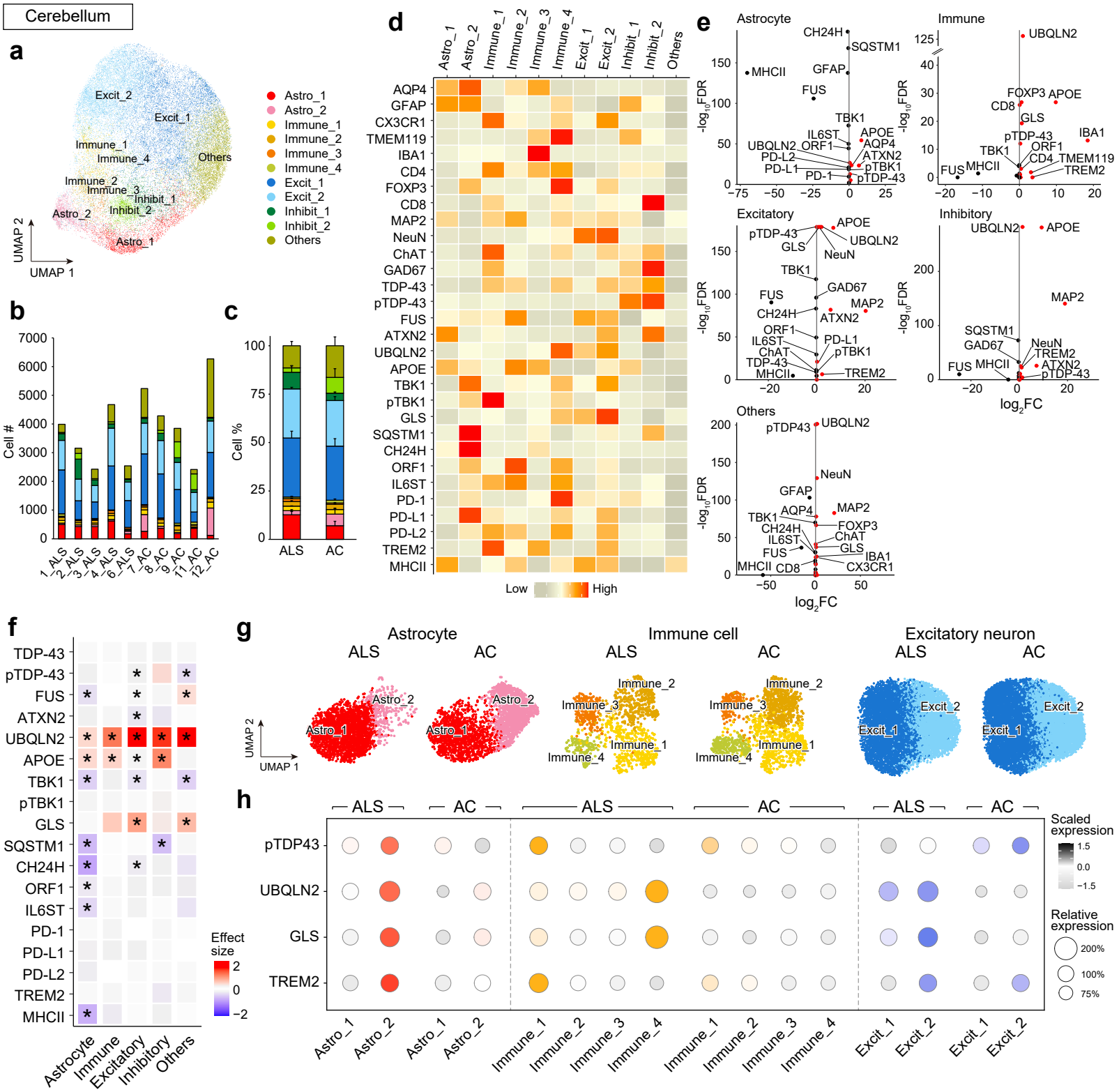

Supplementary Fig. 10 | Single-cell IMC subclassification and indistinct marker expression in the ALS cerebellum.

a, UMAP of IMC-based subclassification in the cerebellum.

b–d, Cell counts of annotated subtypes (**b**), cell proportions (mean ± SEM) (**c**), and marker expression heatmap in which values were Z-score-scaled per marker (**d**) in the cerebellum.

e, Volcano plots of marker protein intensity in astrocytes, immune cells, excitatory neurons, inhibitory neurons, and other populations. Red dots indicate upregulated proteins; black dots represent downregulated proteins.

f, Disease-induced protein expression changes. Asterisks indicate –log10(adjusted *p*-value) × effect size > 10.

g, Reclustering of annotated populations of astrocytes, immune cells, and excitatory neurons.

h, Comparisons of differentially expressed proteins (DEPs) across subclassified cell types. The dot plot shows normalized expression levels derived from the reclustered data. IMC signal intensities were z-scaled across each marker for the color scale, and the mean expression level was set to 100% for circle size representation. Despite inconclusive differences in pTDP-43 expression, each cell type could be reclustered based on UBQLIN2 and GLS expression, suggesting the presence of potentially ALS-associated subpopulations.

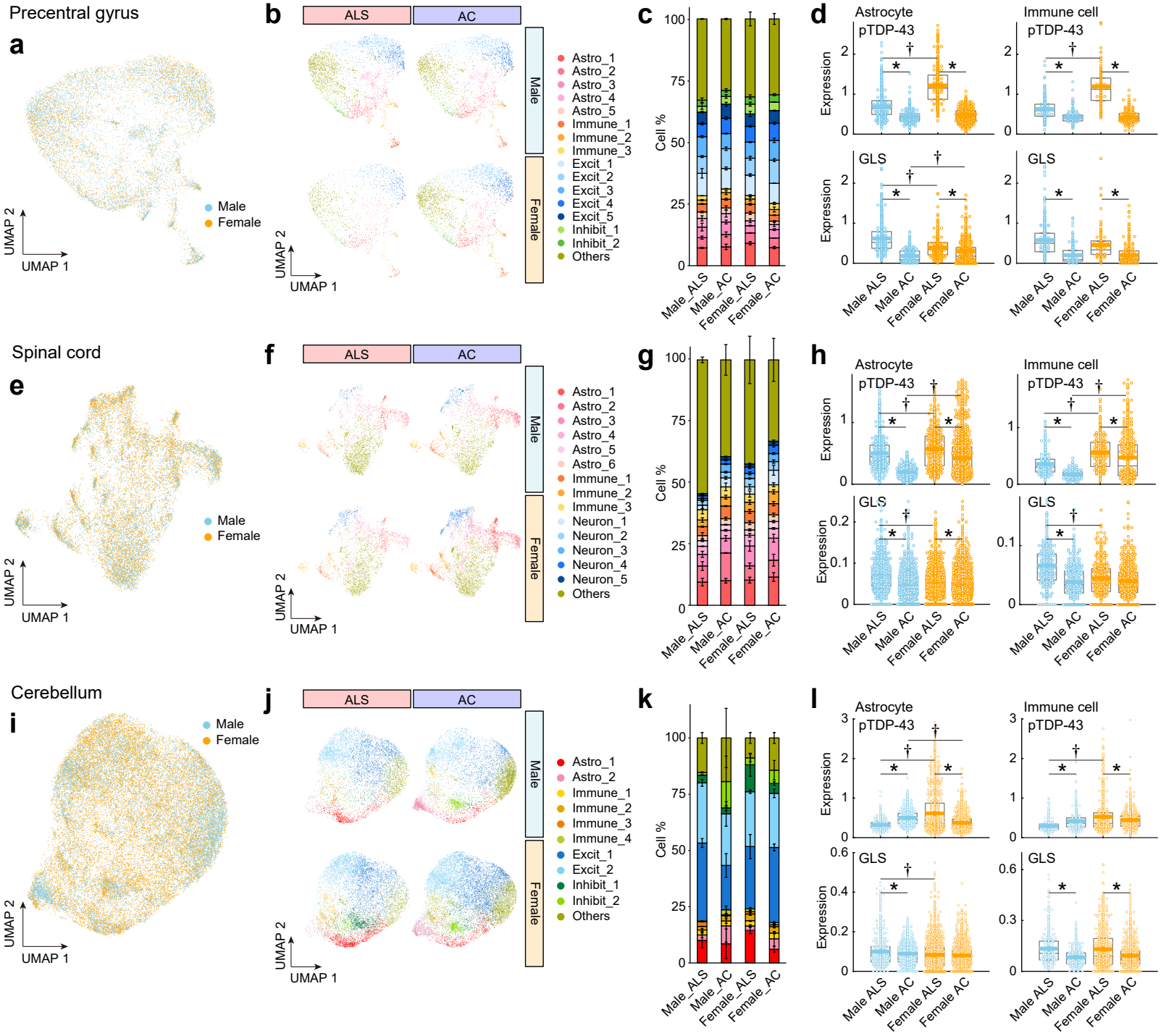

Supplementary Fig. 11 | Comparisons between female and male phenographs in three brain regions.

a, UMAPs of single-cell IMC data from the precentral gyrus gray matter in male and female individuals.

b, Displays of annotated cell subtypes across disease conditions and sexes.

c, Proportions of cell subtypes (mean ± SEM).

d, Expression of pTDP-43 and glutaminase in astrocytes and immune cells.

e–h, Comparisons in the spinal cord.

i–l, Comparisons in the cerebellum.

Statistical analysis was performed using a one-way ANOVA followed by the Tukey-Kramer post hoc test. Asterisks indicate significant differences between ALS and aged control (AC) of the same sex (*$p < 0.001$), and daggers indicate significant differences between males and females under the same condition ($^{\dagger}p < 0.001$) (d, h, and l). Box plots show the median and interquartile range (IQR). The colored horizontal line indicates the mean ± SEM. Each dot represents a single cell.

a Precentral Gyrus

ALS / Aged Control

Iba1(+)

	ALS pTDP-43	ALS GLS	ALS GLS2	ALS p53	Aged Control pTDP-43	Aged Control GLS	Aged Control GLS2	Aged Control p53
Iba1	+++	+++	++	+++	+	+	+	-
pTDP-43		+++	+++	+++		-	-	-
GLS				+++				++
GLS2				++				-

GFAP(+)

	ALS pTDP-43	ALS GLS	ALS GLS2	ALS p53	Aged Control pTDP-43	Aged Control GLS	Aged Control GLS2	Aged Control p53
GFAP	+++	+++	+	+++	++	+	+	+
pTDP-43		+++	++	+++		++	++	++
GLS				++				++
GLS2				-				-

NeuN(+)

	ALS pTDP-43	ALS GLS	ALS GLS2	ALS p53	Aged Control pTDP-43	Aged Control GLS	Aged Control GLS2	Aged Control p53
NeuN	+++	+++	++	++	++	+	+	++
pTDP-43		+++	+++	+++		-	++	++
GLS				+++				+++
GLS2				-				++

Olig2(+)

	ALS pTDP-43	ALS GLS	ALS GLS2	ALS p53	Aged Control pTDP-43	Aged Control GLS	Aged Control GLS2	Aged Control p53
Olig2	+++	-	-	+++	+	-	+	+
pTDP-43		-	++	+++		-	+	+

b Spinal Cord

ALS / Aged Control

Iba1(+)

	ALS pTDP-43	ALS GLS	ALS GLS2	ALS p53	Aged Control pTDP-43	Aged Control GLS	Aged Control GLS2	Aged Control p53
Iba1	+++	+++	-	+++	++	++	+	+
pTDP-43		+++	+	+++		+	-	-
GLS				+++				-
GLS2								

GFAP(+)

	ALS pTDP-43	ALS GLS	ALS GLS2	ALS p53	Aged Control pTDP-43	Aged Control GLS	Aged Control GLS2	Aged Control p53
GFAP	+++	+++	-	+++	++	-	++	++
pTDP-43		+++	-	++		-	+	+++
GLS				+++				-
GLS2				-				-

NeuN(+)

	ALS pTDP-43	ALS GLS	ALS GLS2	ALS p53	Aged Control pTDP-43	Aged Control GLS	Aged Control GLS2	Aged Control p53
NeuN	+++	+++	+	+++	++	++	++	++
pTDP-43		+++	-	+++		++	++	+
GLS				+++				+
GLS2				-				-

Olig2(+)

	ALS pTDP-43	ALS GLS	ALS GLS2	ALS p53	Aged Control pTDP-43	Aged Control GLS	Aged Control GLS2	Aged Control p53
Olig2	+++	-	-	+++	+	-	+	+
pTDP-43		-	++	+++		-	-	+

Supplementary Fig. 12 | Semi-quantitative scoring of protein expression in postmortem human IF.

a,**b**, Semi-quantitative scoring of protein expression in ALS and aged control samples. Confocal immunofluorescence (IF) images were evaluated, based on the co-expression of pTDP-43, GLS, GLS2, and p53 in Iba1(+), GFAP(+), NeuN (+), and Olig2(+) cell types in the precentral gyrus (**a**) and spinal cord (**b**).

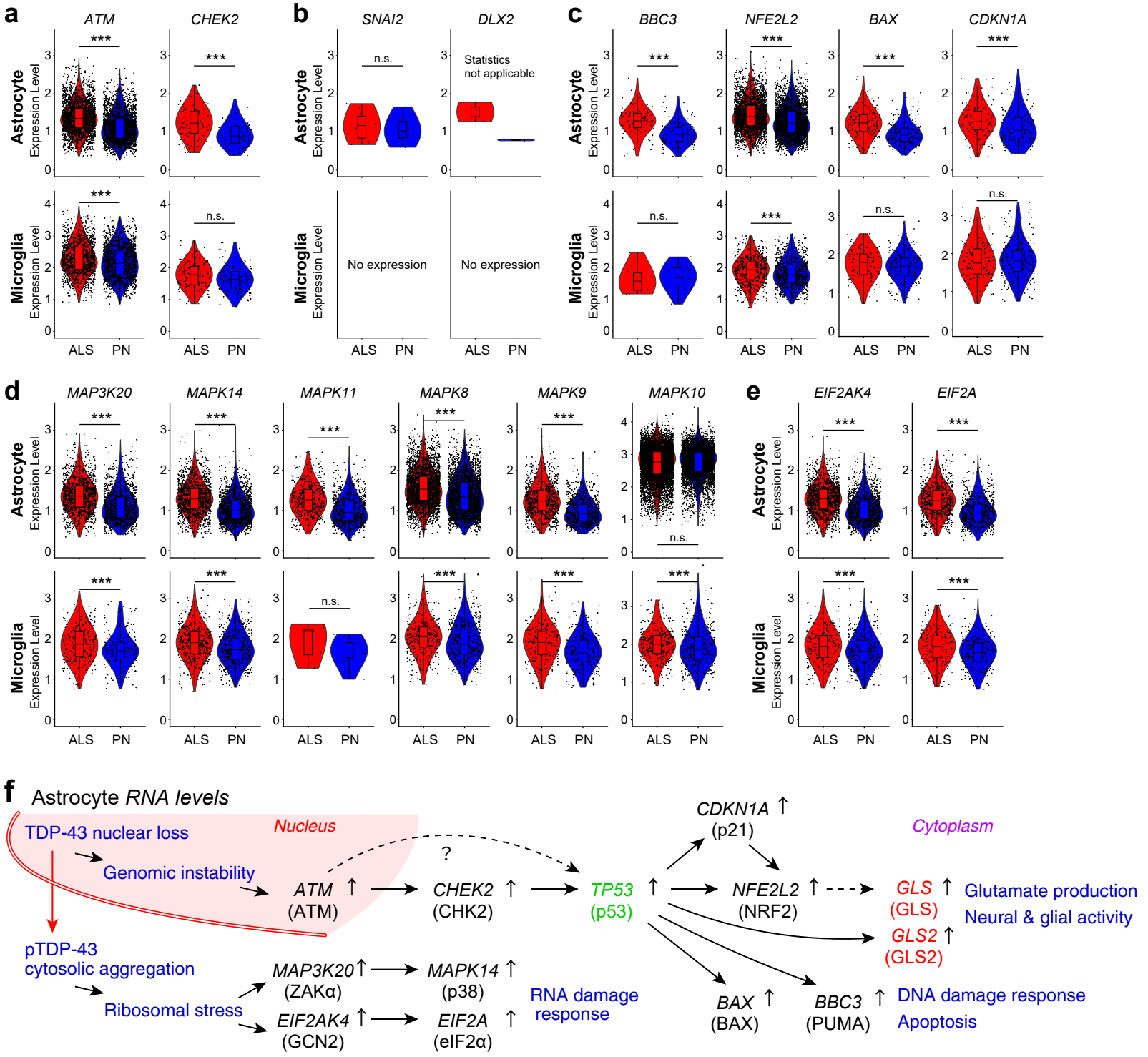

Supplementary Fig. 13 | Transcript associations and a hypothetical model of molecular and cellular mechanisms in sporadic ALS.

a, Increased transcript expression of the p53 positive regulators *ATM* (ATM) and *CHEK2* (CHK2) in cortical astrocytes and microglia from ALS patients (Pineda et al., 2024)[31], supporting the notion of DNA damage responses. Statistical significance is determined by the Wilcoxon rank-sum test with false discovery rate (FDR) correction (***$p < 0.0001$, ALS > PN). Data are means ± SEM; ns, not significant.

b, Transcript expression of the p53 negative regulators *SNAI2* (SLUG) and *DLX2* (DLX2) is unchanged in ALS cortical astrocytes and microglia.

c, Increased transcript expression of the p53 downstream genes *BBC3*, *NFE2L2*, *BAX*, and *CDKN1A* in ALS cortical astrocytes and microglia. Protein products are indicated in parentheses: *BBC3* (PUMA), *NFE2L2* (NRF2), *BAX*, and *CDKN1A* (p21).

d, Increased transcript expression of the ribotoxic stress response-related genes *MAP3K20*, *MAPK14*, and *MAPK11* in ALS cortical astrocytes. JNK encoding transcripts, *MAPK8*, *9*, and *10*, are also increased in ALS astrocytes, supporting the notion of RNA damage responses. Protein products are indicated in parentheses: *MAP3K20* (ZAK), *MAPK14* (p38α), *MAPK11* (p38β), *MAPK8* (JNK1), *MAPK9* (JNK2), *MAPK10* (JNK3). ZAKα is reported to activate p38 MAPK and c-Jun N-terminal kinase (JNK) in the context of ribotoxic stress response in mammals [60, 82].
e, Increased transcript expression of the GCN2-dependent integrated stress response-related genes *EIF2AK4*, and *EIF2A* in ALS cortical astrocytes. Protein products are indicated in parentheses: *EIF2AK4* (GCN2), *EIF2A* (eIF2α). GCN2 activation, acting as a ribosomal collision sensor, is known to phosphorylate eIF2α [60].
f, Hypothetical schema of astrocyte-derived molecular signaling in sporadic ALS, emphasizing transcript-level changes. Loss of nuclear TDP-43 function may activate the DNA damage response pathway, leading to engagement of the p53–glutaminase (GLS) signaling axis. Upregulation of GLS is proposed to enhance glutamate production and extracellular release. Elevated extracellular glutamate may increase neuronal and astrocytic activity, thereby promoting further TDP-43 mislocalization and cytoplasmic translocation [47, 83, 84]. This feed-forward mechanism highlights transcript-level alterations in astrocytes as potential drivers of excitotoxic and TDP-43–associated pathology.

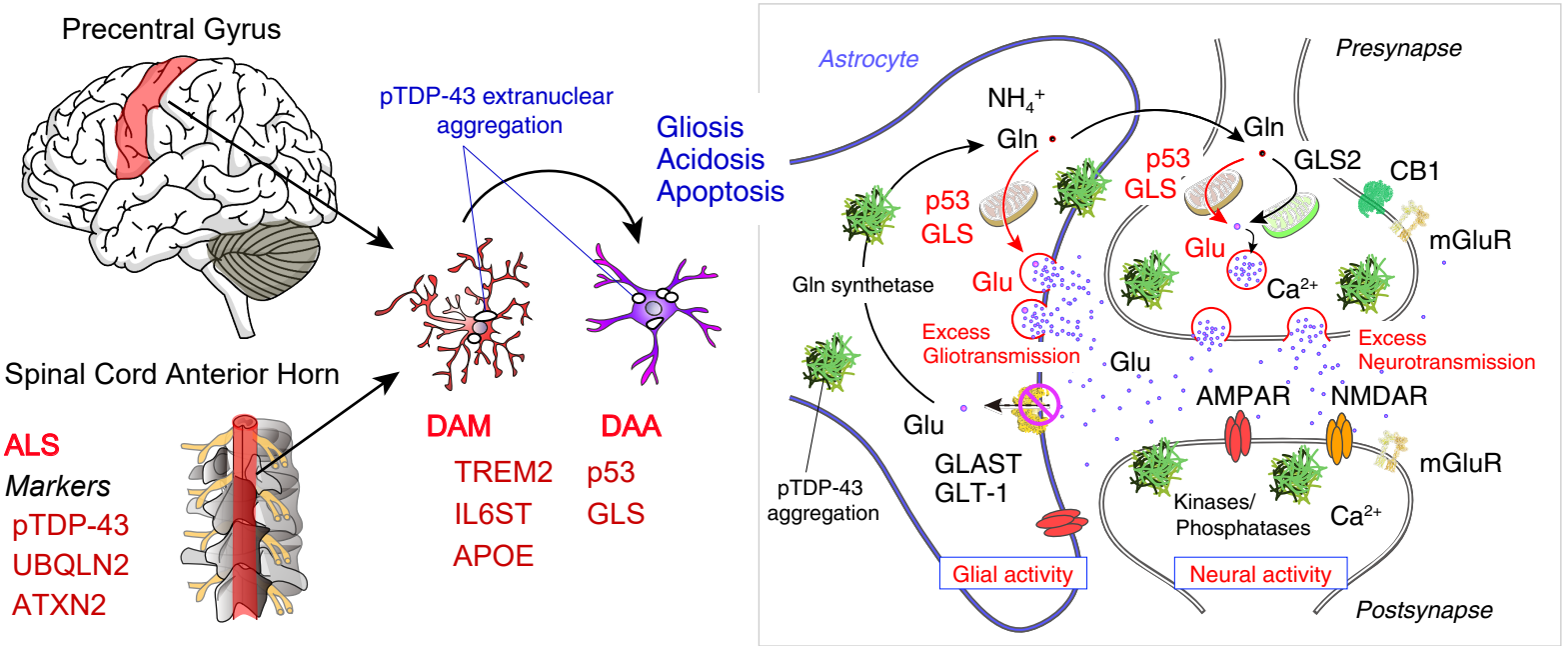

Supplementary Fig. 14 | Transcript associations and a hypothetical model of molecular and cellular mechanisms in sporadic ALS.

Hypothetical cellular model proposed in this study, highlighting glial inflammation associated with RNA stress responses [85].

DONOR #	GROUP	SEX	MILD COGNITIVE IMPAIRMENT	AGE OF DEATH (Y)	DISEASE DURATION (M)	REGION	UNDERLYING CONDITION
1	ALS	F		69	10	Prec (GM+WM), SC, Cereb	
2	ALS	F	MCI	71	12	Prec (GM+WM), SC, Cereb	
3	ALS	F	MCI	69	25	Prec (WM), SC, Cereb	
4	ALS	M		73	20	Prec (GM+WM), SC, Cereb	
†5	ALS	M		70	-		
6	ALS	M		75	24	Prec (GM+WM), SC, Cereb	
7	Aged Control	F		74	0	SC, Cereb	Pancreatic Cancer (PK)
8	Aged Control	F		61	0	Prec (GM+WM), SC, Cereb	Cardiac Pulmonary Arrest on Arrival (CPAOA)
9	Aged Control	F		53	0	Prec (GM+WM), SC, Cereb	CPAOA/Pheochromocytoma
†10	Aged Control	M		54	0		PK
11	Aged Control	M		71	0	Prec (GM+WM), SC, Cereb	Lung Adenocarcinoma
12	Aged Control	M		60	0	Prec (GM+WM), SC, Cereb	Acute Respiratory Distress Syndrome

Supplementary Table 1 | Information on individuals who provided brain samples.

Individuals were categorized as sporadic ALS patients (early-stage ALS, defined as ≤ two years after onset) or age-matched controls (AC) based on clinical diagnosis [80, 81]. All brain samples were obtained from Japanese donors. Mild cognitive impairment (MCI) was identified in two female cases. Information is provided on the age at death, disease duration, and organ regions included in the single-cell analysis. Participants without ALS did not show any ALS-like motor deficits and the clinical diagnosis. Underlying medical conditions of AC individuals are also listed. Daggers (†) indicate samples used for IMC optimization. Single-cell analyses were performed on 4 to 5 samples per group (sporadic ALS and AC). Abbreviations: Prec, precentral gyrus. GM, gray matter. WM, white matter. SC, lumbar spinal cord (anterior horn), Cereb, cerebellar cortex.

						Neuronal loss and gliosis	
DONOR #	**GROUP**	**Clinical phenotype**	**Initial symptom**	**Pathological Diagnosis**	**Brain weight (g)**	**Precentral gyrus**	**Hypoglossal nucleus**
1	ALS	Classical type	Lower limb weakness	ALS-TDP	1110	2	1
2	ALS	Bulbar type	Bulbar palsy	ALS-TDP	1060	1	3
3	ALS	Bulbar type	Bulbar palsy	ALS-TDP	1000	2	3
4	ALS	Classical type	Upper limb weakness and bulbar palsy	ALS-TDP	1170	1	3
5	ALS	Classical type	Lower limb weakness	ALS-TDP	1466	1	1
6	ALS	Classical type	Right upper limb weakness	ALS-TDP	1260	1	1

Supplementary Table 2 | Clinical and neuropathological findings of patients with ALS.

Neuropathological staining results of patients with ALS (cases #1–#6) are presented along with brain weight (in grams). The table summarizes the clinical phenotype, initial symptoms, and pathological diagnoses. It also summarizes findings of neuronal loss and gliosis in the precentral gyrus, hypoglossal nucleus, pyramidal tract, and anterior horn cells of the cervical, thoracic, and lumbar spinal cord. Brettschneider's ALS-TDP stage [1–4] was also assessed [86]. The distribution of pathological markers, identified by histopathological staining, is presented, including NIA-AA AD neuropathologic change (ADNC; Ref. 81), cerebral amyloid angiopathy (CAA), argyrophilic grain disease (AGD; Ref. 87), α-synuclein pathology, and cerebrovascular disease (CVD). According to the NIA-AA ADNC criteria, the ABC score representing the level of Alzheimer's disease neuropathologic change is shown. Neuronal loss and gliosis were semiquantitatively scored as follows: 0 = none, 1 = mild, 2 = moderate, and 3 = severe.

				Aging pathology				
DONOR #	**Anterior horn cells of spinal cord** **Cervical/thoracic/ lumbar cord**	**Pyramidal tract degeneration**	**Brettschneider's ALS-TDP stage** **(Ref 86)**	**NIA-AA AD-NC** **(Ref 81)**	**CAA**	**AGD** **(Ref 87)**	**α-synuclein pathology**	**CVD**
1	2/2/2	2	2	A3B3C1 Intermediate	0	Saito's stage I	0	0
2	2/2/1	1	4	A1B2C1 Low	0	Saito's stage II	0	0
3	3/3/3	3	4	A1 B1C0 Low	0	0	0	0
4	2/2/2	2	4	A3B1C1 Low	1	0	0	0
5	3/3/3	1	1	A0B1C0 Not	0	0	0	0
6	3/3/2	1	2	A0B1C0 Not	0	0	0	0

Supplementary Table 2, continued.

			Aging pathology				
DONOR #	**GROUP**	**Brain weight (g)**	**NIA-AA AD-NC (Ref 81)**	**CAA**	**AGD (Ref 87)**	**α-synuclein pathology**	**CVD**
7	Aged Control	1112	A3B1C0 Low	0	0	0	0
8	Aged Control	1302	A0B1C0 Not	0	0	0	0
9	Aged Control	1318	A0B1C0 Not	0	0	0	0
10	Aged Control	1294	A0B1C0 Not	0	0	0	0
11	Aged Control	1455	A3B2C1 Intermediate	1	0	0	0
12	Aged Control	1460	A0B1C0 Not	0	0	0	0

Supplementary Table 3 | Diagnostic findings based on neuropathological staining in aged control participants.
Neuropathological staining results of aged control participants (cases #7–#12) are shown along with brain weight (in grams). The table summarizes the presence and distribution of pathological markers identified by histopathological staining, including NIA-AA AD neuropathologic change[81], CAA, AGD[87], α-synuclein pathology, and CVD. According to the NIA-AA ADNC criteria, the ABC score indicating the level of Alzheimer's disease neuropathologic change is shown[81]. All participants were clinically diagnosed as neurologically healthy and had no history of neurodegenerative disease. Neuronal loss and gliosis were semiquantitatively scored as follows: 0 = none, 1 = mild, 2 = moderate, and 3 = severe.

Cell Type	*Astrocytes*	*Immune cells*	*Neurons*		*Others*
			(Excitatory)	(Inhibitory)	
Precentral gyrus (Gray matter)	2,515	858	4,300	736	3,772
Lumbar spinal cord	5,556	1,904	1,970		6,913
Cerebellar cortex	5,433	2,712	20,890	3,801	6,016
Precentral gyrus (White matter)	1,238	2,622	1,719		2,377

Supplementary Table 4 | Numbers of classified cells in different regions.

Total numbers of astrocytes, immune cells, excitatory neurons, inhibitory neurons, and unclassified cell populations are listed across four brain regions.

Supplementary References

61. Middeldorp, J. & Hol, E. M. GFAP in health and disease. *Prog. Neurobiol.* **93**, 421–443 (2011). doi: 10.1016/j.pneurobio.2011.01.005.
62. Leipp, F. et al. Glial fibrillary acidic protein in Alzheimer's disease: a narrative review. *Brain Commun.* **6**, fcae396 (2024). doi: 10.1093/braincomms/fcae396.
63. Abdelhak, A. et al. Blood GFAP as an emerging biomarker in brain and spinal cord disorders. *Nat. Rev. Neurol.* **18**, 158–172 (2022). doi: 10.1038/s41582-021-00616-3.
64. Verde, F. et al. Serum levels of glial fibrillary acidic protein in patients with amyotrophic lateral sclerosis. *Ann. Clin. Transl. Neurol.* **10**, 118–129 (2023). doi: 10.1002/acn3.51708.
65. Habib, N. et al. Disease-associated astrocytes in Alzheimer's disease and aging. *Nat. Neurosci.* **23**, 701–706 (2020). doi: 10.1038/s41593-020-0624-8.
66. González de Aguilar, J. L. et al. Alteration of the Bcl-x/Bax ratio in a transgenic mouse model of amyotrophic lateral sclerosis: evidence for the implication of the p53 signaling pathway. *Neurobiol. Dis.* **7**, 406–415 (2000). doi: 10.1006/nbdi.2000.0295.
67. Osorio, D. & Cai, J. J. Systematic determination of the mitochondrial proportion in human and mice tissues for single-cell RNA-sequencing data quality control. *Bioinformatics* **37**, 963–967 (2021). doi: 10.1093/bioinformatics/btaa751.
68. Yu, C. H. et al. TDP-43 Triggers Mitochondrial DNA Release via mPTP to Activate cGAS/STING in ALS. *Cell* **183**, 636–649.e18 (2020). doi: 10.1016/j.cell.2020.09.020.
69. Tanaka, Y. et al. Progranulin regulates lysosomal function and biogenesis through acidification of lysosomes. *Hum. Mol. Genet.* **26**, 969–988 (2017). doi: 10.1093/hmg/ddx011.
70. Tashiro, Y. et al. Motor neuron-specific disruption of proteasomes, but not autophagy, replicates amyotrophic lateral sclerosis. *J. Biol. Chem.* **287**, 42984–42994 (2012). doi: 10.1074/jbc.M112.417600.
71. Root, J. et al. Lysosome dysfunction as a cause of neurodegenerative diseases: Lessons from frontotemporal dementia and amyotrophic lateral sclerosis. *Neurobiol. Dis.* **154**, 105360 (2021). doi: 10.1016/j.nbd.2021.105360.
72. Todd, T. W. et al. The endolysosomal pathway and ALS/FTD. *Trends Neurosci.* **46**, 1025–1041 (2023). doi: 10.1016/j.tins.2023.09.004.
73. Stirling, D. R. et al. CellProfiler 4: improvements in speed, utility and usability. *BMC Bioinformatics* **22**, 1–11 (2021). doi: 10.1186/s12859-021-04344-9.
74. Schapiro, D. et al. histoCAT: analysis of cell phenotypes and interactions in multiplex image cytometry data. *Nat. Methods* **14**, 873–876 (2017). doi: 10.1038/nmeth.4391.
75. Hao, Y. et al. Integrated analysis of multimodal single-cell data. *Cell* **184**, 3573–3587.e29 (2021). doi: 10.1016/j.cell.2021.04.048.
76. Korsunsky, I. et al. Fast, sensitive and accurate integration of single-cell data with Harmony. *Nat. Methods* **16**, 1289–1296 (2019). doi: 10.1038/s41592-019-0619-0.
77. Cao, J. et al. The single-cell transcriptional landscape of mammalian organogenesis. *Nature* **566**, 496–502 (2019). doi: 10.1038/s41586-019-0969-x.
78. Chen, E. Y. et al. Enrichr: interactive and collaborative HTML5 gene list enrichment analysis tool. *BMC Bioinformatics* **14**, 128 (2013). doi: 10.1186/1471-2105-14-128.
79. Subramanian, A. et al. Gene set enrichment analysis: a knowledge-based approach for interpreting genome-wide expression profiles. *Proc. Natl. Acad. Sci. U.S.A.* **102**, 15545–15550 (2005). doi: 10.1073/pnas.0506580102.

80. Arai, T. et al. TDP-43 is a component of ubiquitin-positive tau-negative inclusions in frontotemporal lobar degeneration and amyotrophic lateral sclerosis. *Biochem. Biophys. Res. Commun.* **351**, 602–611 (2006). doi: 10.1016/j.bbrc.2006.10.093.
81. Montine, T. J. et al. National Institute on Aging-Alzheimer's Association guidelines for the neuropathologic assessment of Alzheimer's disease: a practical approach. *Acta Neuropathol.* **123**, 1–11 (2012). doi: 10.1007/s00401-011-0910-3.
82. Robinson, K. S. et al. ZAKα-driven ribotoxic stress response activates the human NLRP1 inflammasome. *Science* **377**, 328–335 (2022). doi: 10.1126/science.abl6324.
83. Weskamp, K., et al. Shortened TDP43 isoforms upregulated by neuronal hyperactivity drive TDP43 pathology in ALS. *J. Clin. Invest.* **130**, 1139–1155 (2020). doi: 10.1172/JCI130988.
84. Park, J. H. et al. Cytosolic calcium regulates cytoplasmic accumulation of TDP-43 through Calpain-A and Importin alpha3. *Elife* **9**, e60132 (2020). doi: 10.7554/eLife.60132.
85. Uemura, K. et al. Glioinflammation: Disease-Associated Microglia and Astrocytes in Psychiatric Disorders, Neurodegeneration, and Senescence. *Front. Cell. Neurosci.* **19**, 1669272 (2026). doi: 10.3389/fncel.2025.1669272.
86. Brettschneider, J. et al. Stages of pTDP-43 pathology in amyotrophic lateral sclerosis. *Ann. Neurol.* **74**, 20–38 (2013). doi: 10.1002/ana.23937.
87. Saito, Y. et al. Staging of argyrophilic grains: an age-associated tauopathy. *J. Neuropathol. Exp. Neurol.* **63**, 911–918 (2004). doi: 10.1093/jnen/63.9.911.